A Real-Time Robust Ecological-Adaptive Cruise Control Strategy for Battery Electric Vehicles

Sheng Yu, Xiao Pan, Anastasis Georgiou, Boli Chen, Imad M. Jaimoukha and Simos A. Evangelou

***Abstract*—This work addresses the ecological-adaptive cruise control problem for connected electric vehicles by a computationally efficient robust control strategy. The problem is formulated in the space-domain with a realistic description of the nonlinear electric powertrain model and motion dynamics to yield a convex optimal control problem (OCP). The OCP is solved by a novel robust model predictive control (RMPC) method handling various disturbances due to modelling mismatch and inaccurate leading vehicle information. The RMPC problem is solved by semi-definite programming relaxation and single linear matrix inequality (sLMI) techniques for further enhanced computational efficiency. The performance of the proposed real-time robust ecological-adaptive cruise control (REACC) method is evaluated using an experimentally collected driving cycle. Its robustness is verified by comparison with a nominal MPC which is shown to result in speed-limit constraint violations. The energy economy of the proposed method outperforms a state-of-the-art time-domain RMPC scheme, as a more precisely fitted convex powertrain model can be integrated into the space-domain scheme. The additional comparison with a traditional constant distance following strategy (CDFS) further verifies the effectiveness of the proposed REACC. Finally, it is verified that the REACC can be potentially implemented in real-time owing to the sLMI and resulting convex algorithm.**

***Index Terms*—Connected and automated vehicle, Eco-driving, Adaptive cruise control, Robust model predictive control, Convex optimisation, Linear matrix inequality.**

ACRONYMS AND NOMENCLATURE

CAV	Connected and Automated Vehicle
CDFS	Constant distance following strategy
(R)EACC	(Robust) Ecological Adaptive Cruise Control
(s/m)LMI	(Single/Multiple) Linear Matrix Inequalities
(R)MPC	(Robust) Model Predictive Control
OCP	Optimal Control Problem
RMS	Root-Mean-Square
RSU	Road Side Unit
SDPR	Semi-Definite Programming Relaxation
V2I	Vehicle-to-Infrastructure
V2V	Vehicle-to-Vehicle
Δt	Time headway between two vehicles
η_p	Powertrain power conversion efficiency factor
κ, Ω, θ	Road curvature, raw rate, and slope angle
a_{RMS}, j_{RMS}	RMS acceleration and jerk
E	Ego vehicle kinetic energy
E_b	Battery energy consumption
F_d	Air-drag resistance
f_d	Coefficient of air-drag resistance
F_g	Gradient force
F_m	Mechanical braking force
F_r	Tyre-rolling resistance
f_r	Coefficient of tyre-rolling resistance
F_t	Powertrain driving force
F_w	Total force acting on the wheels
P_b	Input power drawn from battery
s	Vehicle travelled distance
v, v_l	Ego and leading vehicle velocities

S. Yu, X. Pan, I. M. Jaimoukha and S. A. Evangelou are with the Department of Electrical and Electronic Engineering at Imperial College London, UK (sheng.yu17@imperial.ac.uk, xiao.pan17@imperial.ac.uk, i.jaimouka@imperial.ac.uk, s.evangelou@imperial.ac.uk)

A. Georgiou is with the College of Science & Engineering at University of Minnesota Twin Cities, USA (georg611@umn.edu)

B. Chen is with the Department of Electronic and Electrical Engineering at University College London, UK (boli.chen@ucl.ac.uk)

I. INTRODUCTION

With the growing interest in decarbonisation technologies for mitigating urbanisation and environmental issues, intelligent transportation systems with advanced digitalised, automated and electrified road vehicles have been extensively studied [1]. In particular, with the increasing information and intelligence of the transportation field, connected and autonomous vehicles (CAVs) are rapidly developing for the benefits of reduced pollution, increased traffic efficiency, as well as improved driving safety and comfort [2], [3]. The vehicular ad-hoc networks technology enables CAVs to acquire information of route and other road users through Vehicle-to-Vehicle (V2V) and Vehicle-to-Infrastructure (V2I) wireless communications [4]. The works in [5], [6] address the ecological-adaptive cruise control (EACC) problem by real-time optimisation of the driving efficiency of a CAV in a car-following scenario, which is a common driving scenario during everyday driving. In this circumstance, the driving behaviour of the ego vehicle is highly dependent on the leading vehicle. A velocity change of the leading vehicle may not be responded to properly by a conventional vehicle operated by a human driver [7], thereby leading to unnecessary accelerating/braking or even emergency manoeuvres, which result in additional energy usage [8] and reduced traffic efficiency [9]. To address the above issues, recent research has focused on developing EACC systems in order to improve safety, energy and traffic efficiencies in car-following scenarios [10], [11], [12], [13].

The foundation of solving a practical EACC problem involves an accurately modelled framework of the vehicle dynamics and a computationally efficient algorithm of the control strategy such that the controller can provide optimal control solutions in real-time [14], [15]. The dynamics model includes both longitudinal dynamics and energy consumption models. In the literature, longitudinal dynamic equations can vary from

simplified linear models, which exclude any resistive forces [16] to the more realistic but nonlinear models due to the presence of the nonlinear friction losses, such as the air-drag resistance which is quadratically related to the velocity of the vehicle and the tyre-rolling resistance which exists only when the vehicle speed is nonzero [17]. The main motivation for utilising a simplified linear model is to reduce the computational burden of the scheme. On the other hand, although a more realistic model considers details of the motion, its nonlinearity leads to an extensive computational burden which makes the practical implementation challenging [18], especially for a fast dynamic system such as the car-following one. To overcome the computation issue caused by nonlinearity, [19] defines a synthetic control law, where the nonlinear terms can be compensated by feedback linearisation, such that the vehicle longitudinal dynamic model is linearised. However, feedback linearisation requires accurate knowledge of nonlinear terms [20], while parameters involved in the nonlinear terms of the EACC model such as the air-drag resistance coefficient are usually not known very accurately and may also be changing with travel conditions. In the powertrain modelling aspect, a commonly used energy consumption model is the L^2 norm of the acceleration (control input), which is thought to be monotonically related to the energy consumption [21]. Nevertheless, this simplified model cannot accurately predict energy usage due to the ignorance of the powertrain characteristics, such as the energy conversion and mechanical transmission losses [22], [23]. Alternatively, a battery electric powertrain model is usually taken into account by a quadratic model of the driving force and the velocity, which strikes a balance between modelling accuracy and convexity of the problem [24], [25]. In this context, [25] utilises a sequential quadratic programming method to efficiently solve the nonlinear electric truck platooning optimisation problem by reorganising the problem variables. Moreover, [26] presents a convex scheme for a signal-free autonomous vehicle intersection crossing problem through a coordinate transformation from time- to space-domain and non-conservative relaxation, which can ensure the consistency between original and convexified problems. However, a computationally efficient scheme specialised in the battery electric vehicle powertrain that considers various longitudinal dynamic resistances, as well as electric powertrain conversion and transmission losses, has not been extensively studied in the field of EACC.

In addition to the research on the modelling aspect of the EACC problem, there have been numerous efforts reported in the literature regarding the control strategies of the problem, such as fuzzy control, sliding mode control, learning-based control, and MPC [27], [28], [29], [30], [31], [32], [33]. More specifically, in [27], fuzzy control is employed and then an adaptive law is proposed to control the autonomous vehicle system, which guarantees both deterministic as well as fuzzy performances of the system. An integral sliding mode control strategy is presented in [28] for EACC systems. The method is coupled with a disturbance observer that estimates unknown uncertainties of the vehicular system. In [29], a machine learning-based controller is proposed, which can predict unexpected vehicular behaviours to achieve a resilient control solution. In addition, [30] utilises a deep Q-network algorithm to learn the control strategies for car-following and powertrain energy management with the assistance of a vision-based distance detector. Furthermore, MPC-based methods are also widely studied and applied in the field. Ref [31] proposes a stochastic MPC approach with robust chance constraints, which is addressed by solving the dual problem of the original problem based on the strong duality theory and the semi-definite programming relaxation (SDPR) technique. Ref [32] proposes a novel RMPC concept for a multi-objective adaptive cruise control system provided that the additive disturbances are predictable. This method ensures input-to-state stability by imposing an additional quadratic constraint for the stage and terminal costs in the MPC framework. Moreover, a tube-based MPC is adopted by [33] to cope with uncertainties from non-autonomous vehicles by confining the state and input vectors within tightened feasible sets with a high probability. A feed-forward controller is integrated and triggered in the event of unusually large disturbances. Earlier initial work of the authors, which serves as a precursor of the current work, utilises an RMPC method with SDPR and multiple linear matrix inequality (mLMI) constraints techniques to make progress with addressing the modelling mismatches in the EACC problem [34], [35]. Despite a rich literature and the previous work of the authors on control strategies of the EACC problem, there is still a lack of improvement in computational speed for real-time implementation and robust guarantee against unavoidable disturbances caused by varying system and input parameters.

Based on some preliminary results presented in [34], this paper further addresses the concerns on model accuracy, control robustness, and computation efficiency of the EACC problem through designing a space-domain modelling framework, and developing a robust and convex MPC scheme. Specifically, this paper makes the following contributions:

- It proposes a novel real-time robust ecological-adaptive cruise control (REACC) strategy for an electric CAV, which unlike previous work in the literature and [34], [35] a) utilises a precisely fitted electric powertrain model that considers energy conversion and mechanical transmission losses instead of employing the commonly used L^2 norm of the acceleration [21] or other simplified energy consumption models neglecting losses, b) explicitly defines vehicle dynamic modelling mismatches on air-drag coefficients, tyre-rolling resistance coefficients, and road slope angles rather than adopting Gaussian distributed random disturbances as in previous literature and [34], and c) takes into account the communication or sensing error of the leading vehicle by the dynamic model of the vehicle time gap.
- By the choice of the space-domain, the resulting car-following control problem is newly formulated into a convex optimal control problem (OCP). This is not realisable in the time-domain which is commonly utilised in previous EACC literature [11], [14], [17], [35]. The convex OCP is solved by an LMI-based RMPC technique with a novel combination of features: a) the RMPC tech-

nique is for a system subject to direct additive bounded disturbances, instead of recasting disturbances into uncertainties as in [36], and b) the problem constraints are captured by a single LMI (sLMI) reformulation, which can achieve comparable optimality but with reduced computational complexity compared to the mLMI methods as in [34], [35].

- By comprehensive numerical case studies, the performance of the REACC method is investigated and compared with three benchmarking approaches: a) a nominal (non-robust) MPC scheme that does not consider disturbances in its control framework, b) a recently proposed time-domain convexified and optimal EACC formulation scheme [35], and c) a traditional and non-optimised constant distance following strategy (CDFS) [37]. The proposed method demonstrates improved energy efficiency and a more comfortable travel experience compared to the benchmark algorithms, with guaranteed robustness properties. Furthermore, the computational time of the proposed REACC scheme is evaluated to verify its potential for real-time implementation.

The rest of the paper begins with a statement of the original non-convex EACC problem and modelling in Section II, followed by Section III, which reformulates the original problem into a convex and nominal (disturbance-free) OCP through proper convex relaxation and approximation methods. Moreover, the OCP is rewritten into a condensed nominal MPC format as a benchmark. The proposed RMPC algorithm with SDPR and sLMI (the REACC), which addresses disturbances including the modelling mismatches, is further introduced in Section IV. Simulation results of the REACC and benchmark comparisons are illustrated and discussed in Section V. Finally, conclusions are provided and a future work plan is suggested in Section VI.

Notation: Let $\mathbb{R}$, $\mathbb{R}_{\geq 0}$, $\mathbb{R}_{>0}$ and $\mathbb{N}_{>0}$ denote the real, the non-negative real, the strict positive real sets of numbers, and non-zero natural numbers, respectively. $\mathbb{R}^n$ denotes the space of a n-dimensional real (column) vector, $\mathbb{R}^{n\times m}$ denotes the space of a $n\times m$ real matrix and $\mathbb{D}^n$ denotes the space of a diagonal matrix in $\mathbb{R}^{n\times n}$. I^n denotes an $n\times n$ square matrix with ones on the main diagonal and zeros elsewhere. $\mathbf{0}^{n\times m}$ denotes an $n\times m$ matrix with all zeros. $A^\top$ represents the transpose of A. Let a symmetric matrix $Q\in\mathbb{R}^{n\times n}$ with $Q\succeq 0$ denote a positive semi-definite matrix. For matrices, $Q_1,\ldots,Q_n$, $\text{diag}\{Q_1,\ldots,Q_n\}$ represents a block diagonal matrix with Q_i the i^{th} diagonal matrix.

II. Formulation of EACC problem with uncertainties

This work focuses on the EACC paradigm, where there is an ego CAV (also known as the controlled vehicle) and its driving behaviour is constrained by the traffic in front. As it can be seen in Fig. 1, an ego vehicle is able to acquire real-time road information from GPS or roadside units (RSUs), such as legal speed limit, road curvature, and slope angle, [38], [39]. The front traffic can be reasonably formulated as a leading vehicle [40], and in the present framework, it is assumed that a speed profile of the leading vehicle is available for the ego vehicle, which can be obtained from the leading vehicle via V2V [41] or from the RSUs via V2I [42] communication. Furthermore, it is assumed that no lane changing or overtaking of the leading vehicle is taking place.

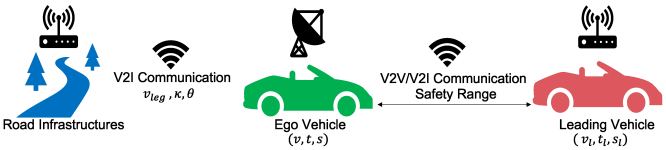

Fig. 1: Scheme of EACC paradigm with V2I and V2V Communications.

In this paper, the ego vehicle is requested to travel the same distance as the leader, which is predefined. However, the following distance gap is not fixed and can vary within a specified range. In this regard, the aim is to design a real-time robust MPC-based EACC strategy that optimises energy consumption with free-end time. In order to make vehicle travel time as a state variable that can be easily optimised, we formulate the problem in the space-domain (also known as spatial-domain) [24] rather than in the time-domain as with the majority of optimisations in adaptive cruise control in the literature. Later on, it will also be shown that the space-domain modelling approach can yield a convex program without sacrificing optimality in terms of the energy economy.

Let us first denote s the vehicle travelled distance, which is the independent variable in the space-domain formulation. Then, the motion of the ego vehicle can be described by the following dynamic equation [24]

$$\frac{d}{ds}E(s) = F_w(s) - F_d(s) - F_r(s) - F_g(s), \tag{1}$$

where $E(s) = \frac{1}{2}mv(s)^2$ is the kinetic energy of the ego vehicle, with $v(s)$ the velocity of the ego vehicle and m the ego vehicle mass, and $F_w(s)$ is the total force acting on the wheels. Note that $E(s)$ is chosen as the state to represent vehicle motion rather than $v(s)$ to avoid the nonlinear dynamic relationship in the space-domain [43]. Moreover, $F_d(s) = \frac{2f_d(s)E(s)}{m}$ is the air-drag resistance, $F_r(s) = mgf_r(s)\cos\theta(s)$ is the tyre-rolling resistance, with g the acceleration of gravity and $f_d(s)$ and $f_r(s)$ the space-dependent coefficients of air-drag and tyre-rolling resistance forces, respectively. Finally, $F_g(s) = mg\sin\theta(s)$ is the gradient force due to the road slope angle $\theta(s)$. Without loss of generality, it is assumed that the nominal values of $f_d(s)$, $f_r(s)$ and $\theta(s)$ are known from the vehicle characteristics, GPS, and so on. Therefore, the real values of $f_d(s)$, $f_r(s)$ and $\theta(s)$ can be represented as

$$\begin{aligned} f_d(s) &= \tilde{f}_d + \Delta f_d(s), \\ f_r(s) &= \tilde{f}_r + \Delta f_r(s), \\ \theta(s) &= \tilde{\theta}(s) + \Delta\theta(s), \end{aligned} \tag{2}$$

where $\tilde{f}_d$, $\tilde{f}_r$, and $\tilde{\theta}$ are the nominal parameters available to CAVs, and $\Delta f_d(s)$, $\Delta f_r(s)$, and $\Delta\theta(s)$ are the unknown parts, treated as modelling mismatch. The mismatch of the real to the nominal air-drag and tyre-rolling resistance coefficients,

respectively, is assumed to be bounded with $f_d(s) \in [\underline{f}_d, \overline{f}_d]$ and $f_r(s) \in [\underline{f}_r, \overline{f}_r]$. The bounds $\underline{f}_d$ and $\overline{f}_d$ of the air-drag resistance coefficient can be determined with reference to the physical relationship between the air-drag resistance coefficient and the headway distance [12], [44]. The tyre-rolling resistance coefficient limits, $\underline{f}_r$ and $\overline{f}_r$, are determined based on the investigation of practical tyre-rolling coefficients at the International Organization for Standardization (ISO) conditions [45]. Furthermore, $\Delta\theta(s)$ represents the gap between the real road slope angle $\theta(s)$ and the nominal angle data $\tilde{\theta}(s)$ collected by road infrastructures including RSUs (which are accessible to CAVs) at the position s. This modelling mismatch on road gradients can be caused by RSU measuring errors, speed humps or other temporary road work. In the present work, the gradient mismatch range is assumed to be a bounded disturbance with $\Delta\theta(s) \in [\underline{\Delta\theta}, \overline{\Delta\theta}]$.

Next, considering $v_l(s)$ the leading vehicle velocity, the dynamics of the time headway between the two vehicles, $\Delta t(s)$, are governed by

$$\frac{d}{ds}\Delta t(s) = \frac{1}{v(s)} - \frac{1}{v_l(s)}. \tag{3}$$

For the sake of further discussion and the introduction of the RMPC framework, the system (1)-(3) is discretised by forward Euler discretisation subject to a sampling interval $\delta s \in \mathbb{R}_{>0}$, leading to the discrete dynamic system

$$E(k+1) = E(k) + \Big(F_w(k) - \frac{2f_d(k)E(k)}{m} - mgf_r(k)\cos\theta(k) - mg\sin\theta(k)\Big)\delta s, \tag{4a}$$

$$\Delta t(k+1) = \Delta t(k) + \left(\frac{1}{\sqrt{2E(k)/m}} - \frac{1}{v_l(k)}\right)\delta s, \tag{4b}$$

where the sampling index $k \in \mathbb{N}_{[0,k_s]}$ with the total number of samples $k_s = S_f/\delta s \in \mathbb{N}_{>0}$ (S_f is the predefined total travelled distance). The boundaries of the permissible range of the time gap are constructed below

$$\Delta t_{\min} \le \Delta t(k) \le \Delta t_{\max}, \tag{5}$$

where $\Delta t_{\min}$ is the minimum time gap to avoid rear-end collision, and $\Delta t_{\max}$ is the maximum allowed time gap to improve traffic capacity and maintain adequate V2V/V2I communication. For safety purposes, the kinetic energy $E(k)$ is bounded by

$$E_{\min} \le E(k) \le E_{\max}(k), \tag{6}$$

where $E_{\min} = \frac{1}{2}mv_{\min}^2$ and $E_{\max}(k) = \frac{1}{2}mv_{\max}^2(\kappa(k))$ are the lower and upper bounds of kinetic energy, determined by the minimum allowed speed $v_{\min}$, which is a sufficiently small positive constant aiming to avoid the singularity issues in (3) without sacrificing the generality of the formulation, and the maximum speed limit $v_{\max}(\kappa(k))$. Note that $v_{\max}(\kappa(k))$ is modelled as a function of the real-time road curvature $\kappa(k)$ to ensure safety and comfort during cornering. It is estimated by the concept of the acceleration diamond [46] that represents a combined longitudinal and lateral acceleration constraint for ordinary driving behaviour

$$\left|\frac{F_w(k)/m}{a_{x,\max}}\right| + \left|\frac{v(k)\Omega(k)}{a_{y,\max}}\right| \le 1, \tag{7}$$

where $\Omega(k) = v(k)\kappa(k)$ represents the yaw rate of the vehicle, and $F_w(k)/m$ and $v(k)\Omega(k)$ are the longitudinal and lateral accelerations, and their individual limits are denoted by $a_{x,\max}$ and $a_{y,\max}$, respectively. By reorganising the cornering speed limit (7) and merging the local legal speed limit, $v_{leg}(k)$, the overall combined speed limit of the road, $v_{\max}(v_{leg}(k), \kappa(k))$ can be determined, and hence leads to the constraints on vehicle velocity $v(k)$ as

$$v_{\min} \le v(k) \le \underbrace{\min\left(v_{leg}(k), \sqrt{\left(1 - \frac{F_{w,\max}/m}{a_{x,\max}}\right)\frac{a_{y,\max}}{\kappa(k)}}\right)}_{v_{\max}(v_{leg}(k),\kappa(k))}, \tag{8}$$

and the constraints on $E(k)$ in (6) as $E_{\min} = \frac{1}{2}mv_{\min}^2$ (as previously) and $E_{\max}(k) = \frac{1}{2}mv_{\max}^2(v_{leg}(k), \kappa(k))$. $F_{w,\max}$ is the maximum force that can be provided by the vehicle powertrain (see (10) below) to the wheels. During the driving task, the ego CAV can be informed $v_{\min}$ and $v_{\max}(v_{leg}(k), \kappa(k))$ from the infrastructure through the V2I communication.

Moreover, the ego vehicle is assumed to be equipped with a battery-electric powertrain, which is illustrated in Fig. 2. The powertrain connects the battery (energy source) to the driving wheels (loads) through a series of components including a DC-DC converter, a DC-AC converter (an inverter), a permanent magnet synchronous (PMS) machine (motor/generator), and a mechanical transmission set that delivers the powertrain driving force, F_t, to the wheels. Both the converters and the transmission set can be simply modelled by constant efficiency factors [46] (see Table. I), while the efficiency of the PMS machine is modelled as a look-up table-based static efficiency map from ADVISOR [47], with the machine characteristics shown in Table. I. Also, an equivalent circuit model with a constant open circuit voltage, while considering the battery internal resistance, is utilised to model the battery (battery specifics are provided in Table. I) [46].

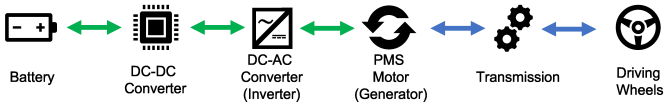

Fig. 2: Block diagram of the battery electric vehicle powertrain with a DC-DC converter, a DC-AC converter (an inverter), a PMS motor (a generator), and a mechanical transmission set. Green and blue arrows represent electrical and mechanical power flows, respectively.

The total force applied on the wheels $F_w(k)$ consists of the powertrain driving force $F_t(k) \in [F_{t,\min}, F_{t,\max}]$ and the non-regenerative (dissipative) mechanical braking force $F_m(k) \in [F_{m,\min}, 0]$ such that

$$F_w(k) = F_t(k) + F_m(k), \tag{9}$$

TABLE I: BATTERY ELECTRIC VEHICLE POWERTRAIN MAIN PARAMETERS.

Descriptions	Symbols	Values
Battery open circuit voltage		432 V
Battery internal resistance		0.12 Ω
Battery package overall capacity		20.736 kWh
DC-DC converter efficiency		0.97
DC-AC converter efficiency		0.96
PMS machine state resistance		90 Ω
PMS machine rotor magnetic flux		0.21 Wb
PMS machine number of poles		6
Transmission efficiency		0.96
Minimum powertrain driving force	$F_{t,\min}$	-3500 N
Maximum powertrain driving force	$F_{t,\max}$	3500 N
Largest mechanical braking force	$F_{m,\min}$	-4300 N
Fitted coefficients of battery terminal power	$a_1/a_2/a_3$	6.31×10^{-5}/ 1.046/115.2

and $F_w(k)$ is subject to the following constraints

$$F_{t,\min} + F_{m,min} \leq F_w(k) \leq F_{t,\max}, \tag{10}$$

with $F_{t,\max}$ ($=F_{w,\max}$) and $F_{t,\min}$ the maximum traction force and largest (negative) regenerative braking force, respectively, delivered by the electric machine at the wheels, and $F_{m,\min}$ the largest (negative) mechanical braking force at the wheels, assuming that the tyres can provide this range of forces.

Therefore, the battery energy consumption (E_b) of the battery electric vehicle can be evaluated by its battery energy usage, whose rate is the input power drawn from the battery to drive the vehicle, P_b. The power P_b can be further represented as a look-up table of F_t and ego vehicle velocity v, $P_b(F_t(k), v(k))$, which is shown in Fig. 3a.

The overall electrical-mechanical power conversion efficiency factor η_p of the battery-electric powertrain is defined as

$$\eta_p(k) = \begin{cases} \dfrac{F_t(k)v(k)}{P_b(k)}, & \forall F_t(k) \geq 0, \\ \dfrac{P_b(k)}{F_t(k)v(k)}, & \forall F_t(k) < 0, \end{cases} \tag{11}$$

which will be employed in Section V to evaluate the ecological performance of the proposed method. Fig. 3b illustrates the overall powertrain efficiency map of η_p, together with the operation limits of the electric machine and powertrain utilised in this work, respectively.

The proposed REACC method in this work aims to save travelling time while reducing energy consumption. Therefore, a tentative non-convex multi-objective stage cost function of the EACC problem is designed as follows

$$L(k) = W_E(E(k) - E_{\max}(k))^2 + W_F \frac{P_b(k)}{v(k)}, \tag{12}$$

where $W_E, W_F \in \mathbb{R}_{>0}$ are two weighting factors. In particular, the first term of the cost function encourages the ego vehicle to maximise mobility, which is equivalent to following $v_{\max}(k)$ as in the time-domain framework, whereas the second term aims to minimise the battery energy usage ($E_b(k)$) under the space-domain, which is determined by $E_b(k) = \frac{P_b(k)}{v(k)}\delta s$.

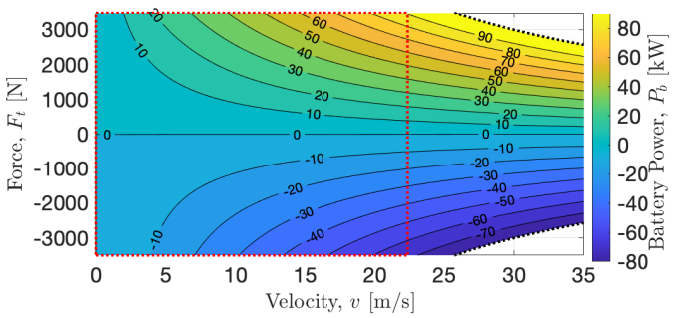

(a) Battery electric vehicle power consumption map.

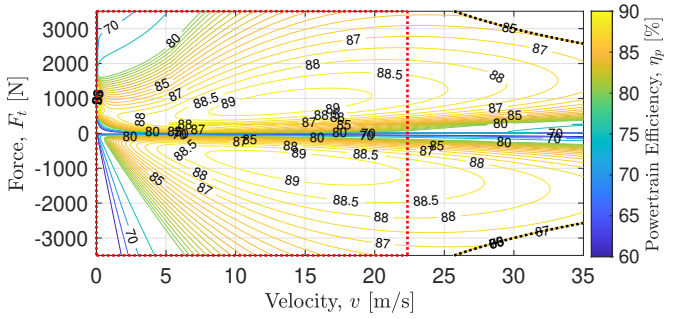

(b) Battery electric vehicle powertrain efficiency map.

Fig. 3: Battery electric vehicle power consumption, P_b (shown in Fig. 3a) and powertrain efficiency, η_p (shown in Fig. 3b), associated with powertrain driving force, F_t and vehicle velocity, v. Positive force means the battery is discharging while negative force indicates the battery is recharging. Solid lines in Fig. 3a and Fig. 3b are battery power consumption and efficiency contour lines, respectively. Black dashed lines are motor operational bounds. Red dashed rectangles denote the feasible overall vehicle powertrain operating range which is determined by the minimum and maximum powertrain driving forces ($F_{t,\min}$ and $F_{t,\max}$), as well as the minimum and maximum velocities ($v_{\min}$ and $v_{\max}$, where for illustration purposes the highest value of v_{leg} is shown for $v_{\max}$ in Fig. 3).

III. EACC PROBLEM CONVEXIFICATION

This section convexifies the formulation of the realistic (with modelling mismatches) EACC problem introduced in Section II and hence reformulates the problem as a convex OCP. The convex modelling framework is then used to design the computationally efficient RMPC in Section IV.

For the sake of further discussion, let us rewrite the system equation (4a) in the following form with separated nominal dynamics and additive disturbance

$$\begin{aligned} E(k+1) = E(k) + \Bigg(& F_w(k) - \frac{2\tilde{f}_d E(k)}{m} \\ & - mg\tilde{f}_r \cos\tilde{\theta}(k) - mg\sin\tilde{\theta}(k) + d_E(k) \Bigg) \delta s, \end{aligned} \tag{13}$$

where $\underline{d}_E \leq d_E(k) \leq \overline{d}_E$ is the disturbance capturing the modelling mismatches existing in both the resistance force coefficients and the road slope angle. Furthermore, the utilisation of time gap Δt as the system state allows the communication or the sensing error of the leading vehicle velocity to be directly

involved in the system dynamics (4b), and hence (4b) can be rewritten as

$$\Delta t(k+1) = \Delta t(k) + \left(\frac{1}{\sqrt{2E(k)/m}} - \frac{1}{\tilde{v}_l(k)} + d_t(k) \right) \delta s, \quad (14)$$

where $\underline{d}_t \leq d_t(k) \leq \overline{d}_t$ is the bounded communication or sensing error of the leading vehicle. Both $d_E(k)$ and $d_t(k)$ will be further explicitly defined in Section IV below.

To deal with the nonlinearity of $\frac{1}{\sqrt{2E(k)/m}}$ existing in the dynamics of (14) due to the space-domain formulation, an auxiliary variable denoted as $\zeta(k)$ is introduced to convexify the nonlinearity. By defining $\zeta(k) = \frac{1}{\sqrt{2E(k)/m}}$, the dynamics of the time gap (14) can be relaxed as an equality constraint and a convex path constraint

$$\Delta t(k+1) = \Delta t(k) + \left(\zeta(k) - \frac{1}{\tilde{v}_l(k)} + d_t(k) \right) \delta s, \quad (15a)$$

$$\zeta(k) \geq \frac{1}{\sqrt{2E(k)/m}}. \quad (15b)$$

Note that the feasibility of the original nominal state dynamics (14) is enlarged in (15a) due to the inequality path constraint (15b). The equivalence between (14) and (15) is valid if the equality of (15b) holds for all k, which can be ensured under the proposed framework and will be discussed below when introducing the stage cost function.

Therefore, by collecting (13) and (15a), a realistic and convex dynamic state-space representation with additive disturbances can be summarised as

$$\begin{aligned} &x(k+1) = Ax(k) + B_u u(k) + B_c C(k) + B_d d(k), \\ &A = \begin{bmatrix} 1 - \frac{2\tilde{f}_d}{m}\delta s & 0 \\ 0 & 1 \end{bmatrix}, B_u = \begin{bmatrix} \delta s & 0 \\ 0 & \delta s \end{bmatrix}, B_c = \begin{bmatrix} \delta s & 0 \\ 0 & \delta s \end{bmatrix}, \\ &C(k) = \begin{bmatrix} -mg\tilde{f}_r \cos\tilde{\theta}(k) - mg\sin\tilde{\theta}(k) \\ -\frac{1}{\tilde{v}_l(k)} \end{bmatrix}, B_d = \begin{bmatrix} \delta s & 0 \\ 0 & \delta s \end{bmatrix}, \end{aligned} \quad (16)$$

where $x(k) = [E(k), \Delta t(k)]^\top$ denotes the realistic state vector, $u(k) = [F_w(k), \zeta(k)]^\top$ is the control input, and $d(k) = \begin{bmatrix} d_E(k) \\ d_t(k) \end{bmatrix}$ collects the disturbances. Note that $C(k)$ depends only on k since both the nominal road slope angle $\tilde{\theta}(k)$ and the available leading vehicle speed $\tilde{v}_l(k)$ contained by $C(k)$ are varying with k. Furthermore, realistic constraints of the states and the input $F_w(k)$ can be given by

$$\underline{f}(k) \leq f(x(k), u(k), d(k)) \leq \overline{f}(k), \quad (17)$$

in which $f(k)$ collects (5) (6), and (10) as given below

$$\begin{aligned} &f(k) = C_f x(k) + D_{fu} u(k) + D_{fd} d(k), \\ &f(k) = \begin{bmatrix} E(k) \\ \Delta t(k) \\ F_w(k) \end{bmatrix}, C_f = \begin{bmatrix} 1 & 0 \\ 0 & 1 \\ 0 & 0 \end{bmatrix}, D_{fu} = \begin{bmatrix} 0 & 0 \\ 0 & 0 \\ 1 & 0 \end{bmatrix}, \end{aligned} \quad (18)$$

with $D_{fd} = \mathbf{0}^{3\times 2}$. $f(k)$ is bounded by lower and upper constraints $\underline{f}(k) = [E_{\min}, \Delta t_{\min}, F_{t,\min} + F_{m,min}]^\top$ and $\overline{f}(k) = [E_{\max}(k), \Delta t_{\max}, F_{t,\max}]^\top$, respectively.

Moreover, it is worth noticing from Fig. 3a that the battery terminal power P_b can be precisely fitted by a quadratic function of F_t and v, as shown in Fig. 4, in which

$$P_b(k) = \left(a_1 F_t(k)^2 + a_2 F_t(k) + a_3 \right) v(k), \quad (19)$$

where a_1, a_2 and a_3 are the fitted coefficients, which are provided in Table. I.

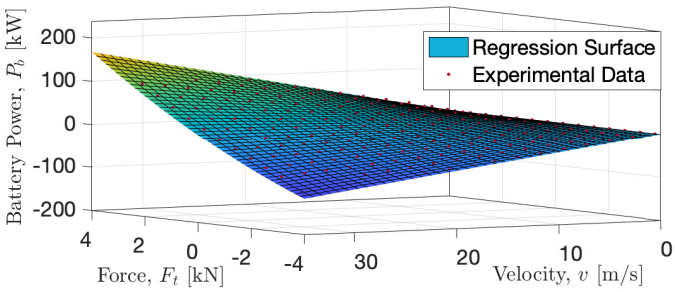

Fig. 4: Electric vehicle battery power fitting map by the quadratic function in (19). Nonlinear regression of the battery-drawn power data represented by the blue regression surface, calculated based on the power consumption map shown in Fig. 3a, with the coefficient of determination, $R^2 = 0.995$.

By substituting (19) into (12) for $P_b(k)$, the multi-objective stage cost function of the EACC problem is convexified as a quadratic polynomial function of $E(k)$ and $F_t(k)$. Moreover, in order to guarantee the inequality condition of (15b) becomes an equality condition once the proposed OCP is formulated, an additional cost $W_\zeta \zeta(k)$ is added to the objective function, with $W_\zeta \in \mathbb{R}_{>0}$ the corresponding weighting factor. The previous non-convex form of the stage cost (12) is finally modified as

$$\begin{aligned} L(k) =& W_E \left(E(k) - E_{\max}(k) \right)^2 \\ &+ W_F \left(a_1 F_w(k)^2 + a_2 F_w(k) \right) + W_\zeta \zeta(k), \end{aligned} \quad (20)$$

which is the final convexified objective function as a quadratic polynomial function of the state $E(k)$ and control inputs $F_w(k)$ and $\zeta(k)$. Term a_3 in (19) is removed since it is a constant term, and $F_t(k)$ is substituted by $F_w(k)$, which are equivalent if there is no mechanical friction braking; see (9). The proof of the equality condition of (15b) by the choice of the stage cost (20) can be referred to the authors' previous work in [26], which involves a similarly convexified stage cost for a different application and is therefore omitted. As the powertrain driving force $F_t(k)$ is replaced by $F_w(k)$ that also includes the mechanical friction braking force, the optimality of the convex optimisation problem that will be formulated may be compromised in case the friction braking force is active during the mission (i.e., $\exists k$, $F_m(k) \neq 0$). However, friction braking is naturally suppressed in eco-driving to maximise energy recovery, which will also be confirmed by the simulation results in Section V.

To summarise, the overall EACC problem with modelling mismatches can be formulated as a convex OCP in the space-domain as follows

$$\min_{u(k)} \quad \sum_{k=0}^{k_s} J(k)\delta s = \left(\sum_{k=0}^{k_s - 1} L(k)\delta s + \Psi(k_s) \right), \quad (21a)$$

$$\textbf{s.t. } x(k+1) = Ax(k) + B_u u(k) + B_c C(k) + B_d d(k), \quad (21b)$$

$$\underline{f}(k) \le f(x(k), u(k), d(k)) \le \overline{f}(k), \quad (21c)$$

$$\zeta(k) \ge \frac{1}{\sqrt{2E(k)/m}}, \quad (21d)$$

$$\begin{bmatrix} \underline{d}_E \\ \underline{d}_t \end{bmatrix} \le d(k) \le \begin{bmatrix} \overline{d}_E \\ \overline{d}_t \end{bmatrix}, \quad (21e)$$

$$\textbf{given: } x(0) = [E(0), \Delta t(0)]^\top, \quad (21f)$$

where $E(0)$ and $\Delta t(0)$ are the system initial states, which are available in advance. $\Psi(k_s)$ is the terminal cost, which is given by

$$\Psi(k_s) = W_E(E(k_s) - E_{\max}(k_s))^2 + W_{\Delta t}(\Delta t(k_s) - \Delta t(0))^2, \quad (22)$$

where the $W_{\Delta t} \in \mathbb{R}_{>0}$ term in the terminal cost $\Psi(k_s)$ is imposed to ensure the distance travelled by the ego vehicle is identical to that of the leading vehicle, thereby facilitating the comparison between different methods. In practice, the $W_{\Delta t}$ term in $\Psi(k_s)$ could be removed or reduced to allow more emphasis on energy economy (more travel time / less energy consumption, since $\Delta t(k_s)$ will tend to $\Delta t_{\max}$) or mobility (less travel time / more energy consumption, since $\Delta t(k_s)$ will tend to $\Delta t_{\min}$), depending on the choice of W_E and W_F.

Furthermore, $J(k)$ of the objective function (21a) can be redefined as a state-space form of a combination of both the stage cost $L(k)$ (20) and the terminal cost $\Psi(k_s)$ (22), and it is expressed by

$$J(k) = (z(k) - \overline{z}(k))^\top Q^\top Q(z(k) - \overline{z}(k)) + Pz(k) + z(k)^\top P^\top, \quad (23)$$

where $z(k) = [E(k), \Delta t(k), F_w(k), \zeta(k)]^\top$ and the reference signal $\overline{z}(k) = [E_{\max}(k), \Delta t(0), 0, 0]^\top$. Furthermore, $z(k)$ can be explicitly expressed as

$$\begin{aligned} z(k) &= C_z x(k) + D_{zu} u(k) + D_{zd} d(k), \quad D_{zd} = \mathbf{0}^{4\times 2}, \\ C_z &= \begin{bmatrix} 1 & 0 & 0 & 0 \\ 0 & 1 & 0 & 0 \end{bmatrix}^\top, \quad D_{zu} = \begin{bmatrix} 0 & 0 & 1 & 0 \\ 0 & 0 & 0 & 1 \end{bmatrix}^\top. \end{aligned} \quad (24)$$

The weighting matrices in (23) are defined as

$$Q(W_{\Delta t}) = \begin{bmatrix} \sqrt{W_E} & 0 & 0 & 0 \\ 0 & \sqrt{W_{\Delta t}} & 0 & 0 \\ 0 & 0 & \sqrt{W_F a_1} & 0 \\ 0 & 0 & 0 & 0 \end{bmatrix}, P = \begin{bmatrix} 0 \\ 0 \\ \frac{1}{2} W_F a_2 \\ \frac{1}{2} W_\zeta \end{bmatrix}, \quad (25)$$

where the Q matrix is dependent on $W_{\Delta t}$, while P is a fixed matrix.

IV. Robust Model Predictive Controller Design for EACC

This section mainly presents the proposed RMPC controller, while a nominal MPC benchmark is also presented.

A. Proposed RMPC algorithm

This subsection designs the proposed RMPC controller for solving the convex OCP (21) in real-time with consideration of two types of disturbances, including the modelling mismatches in the longitudinal dynamics (4a) and the errors involved in the leading vehicle velocity (e.g., caused by communication or sensing) in the dynamics of the time gap (4b) (proposed REACC scheme). The robust optimal solutions are solved by using SDPR and sLMI methods [36].

In view of (4a) and (13), the modelling mismatch in the longitudinal dynamics is explicitly defined as

$$\begin{aligned} d_E(k) = &\left(\tilde{f}_d - f_d(k)\right) \frac{2E(k)}{m} \\ &+ mg\tilde{f}_r \cos\tilde{\theta}(k) + mg\sin\tilde{\theta}(k) \\ &- mgf_r(k)\cos\theta(k) - mg\sin\theta(k), \end{aligned} \quad (26)$$

recalling $\underline{d}_E \le d_E(k) \le \overline{d}_E$ with $\underline{d}_E = \min(d_E(k))$ and $\overline{d}_E = \max(d_E(k))$, which are determined through a conservative consideration of the limits of $f_d(k)$, $f_r(k)$, $\Delta\theta(k)$. Regarding the dynamics of the time gap, its associated error can be defined explicitly after finding the difference between (4b) and (14) as

$$d_t(k) = \frac{1}{\tilde{v}_l(k)} - \frac{1}{v_l(k)}, \quad (27)$$

recalling $\underline{d}_t \le d_t(k) \le \overline{d}_t$, and $\underline{d}_t = \min\left(\frac{1}{\tilde{v}_l(k)} - \frac{1}{v_l(k)}\right)$ and $\overline{d}_t = \max\left(\frac{1}{\tilde{v}_l(k)} - \frac{1}{v_l(k)}\right)$.

For the purpose of saving the computational time as well as the memory requirements [48], the convex OCP formulation (21) is now reorganised into a condensed formulation. Let us define the following stacked vectors

$$\begin{aligned} \mathbf{u} &= [u(0)^\top, u(1)^\top, \ldots, u(N-1)^\top]^\top \in \mathbb{R}^{2N}, \\ \mathbf{C} &= [C(0)^\top, C(1)^\top, \ldots, C(N-1)^\top]^\top \in \mathbb{R}^{2N}, \\ \mathbf{d} &= [d(0)^\top, d(1)^\top, \ldots, d(N-1)^\top]^\top \in \mathbb{R}^{2N}, \\ \overline{\mathbf{d}} &= [\overline{d}^\top, \overline{d}^\top, \ldots, \overline{d}^\top]^\top \in \mathbb{R}^{2N}, \\ \underline{\mathbf{d}} &= [\underline{d}^\top, \underline{d}^\top, \ldots, \underline{d}^\top]^\top \in \mathbb{R}^{2N}, \\ \xi &= [\xi(0)^\top, \xi(1)^\top, \ldots, \xi(N)^\top]^\top, \end{aligned} \quad (28)$$

where N is the prediction horizon length of the MPC problem. $\overline{d}$ and $\underline{d}$ collect disturbance boundaries as $\overline{d} = [\overline{d}_E, \overline{d}_t]^\top$ and $\underline{d} = [\underline{d}_E, \underline{d}_t]^\top$, respectively. The symbol ξ stands for stacked vectors $\mathbf{x}$, $\check{\mathbf{x}}$, $\mathbf{f}$, $\check{\mathbf{f}}$, $\underline{\mathbf{f}}$, $\overline{\mathbf{f}}$, $\mathbf{z}$, $\check{\mathbf{z}}$, and $\overline{\mathbf{z}}$, with $\mathbf{x}$ and $\check{\mathbf{x}} \in \mathbb{R}^{2(N+1)}$, $\mathbf{f}$, $\check{\mathbf{f}}$, $\underline{\mathbf{f}}$, and $\overline{\mathbf{f}} \in \mathbb{R}^{3(N+1)}$, while $\mathbf{z}$, $\check{\mathbf{z}}$ and $\overline{\mathbf{z}}$ lie in $\mathbb{R}^{4(N+1)}$.

As such, the system dynamics (16) over the prediction horizon N can be rewritten into a condensed formulation as

$$\mathbf{x} = \widetilde{A}x(0) + \widetilde{B}_u \mathbf{u} + \widetilde{B}_c \mathbf{C} + \widetilde{B}_d \mathbf{d}, \quad (29)$$

where $x(0)$ is the initial condition defined in (21f), and $\widetilde{A}$, $\widetilde{B}_u$, $\widetilde{B}_c$, and $\widetilde{B}_d$ are stacked coefficient matrices of A, B_u, B_c, and B_d respectively. They are readily obtained from iterating the dynamics in (16) from $k = 0$ to $k = N$.

By repeating the recursive steps in (18) and substituting recursive steps in (16) to eliminate the $x(k)$ terms, the stacked coefficient matrices $\widetilde{C}_f$, $\widetilde{D}_{fu}$, $\widetilde{D}_{fc}$, and $\widetilde{D}_{fd}$ are obtained, and hence the corresponding condensed form of the signal response function of constraint (18) can be written after substituting the stacked vectors defined in (28) as

$$\mathbf{f} = \widetilde{C}_f x(0) + \widetilde{D}_{fu} \mathbf{u} + \widetilde{D}_{fc} \mathbf{C} + \widetilde{D}_{fd} \mathbf{d}, \quad (30)$$

from which it follows that $\underline{\mathbf{f}} \le \mathbf{f} \le \bar{\mathbf{f}}$. Analogously, the condensed form of the cost response function defined in (24) can be expressed by

$$\mathbf{z} = \widetilde{C}_z x(0) + \widetilde{D}_{zu}\mathbf{u} + \widetilde{D}_{zc}\mathbf{C} + \widetilde{D}_{zd}\mathbf{d}, \tag{31}$$

where $\widetilde{C}_z$, $\widetilde{D}_{zu}$, $\widetilde{D}_{zc}$, and $\widetilde{D}_{zd}$ are stacked coefficient matrices after iterating the $z(k)$ equation in (24) and substituting the $x(k)$ equation in (16).

Hence, the stacked formulation of the objective function (23) over a prediction horizon N can be derived by $\mathbf{J}$ with

$$\mathbf{J} = (\mathbf{z}-\bar{\mathbf{z}})^\top \mathbf{Q}^\top \mathbf{Q}(\tilde{\mathbf{z}}-\bar{\mathbf{z}}) + \mathbf{P}\mathbf{z} + \mathbf{z}^\top \mathbf{P}^\top, \tag{32}$$

where $\mathbf{Q} = \mathrm{diag}\{Q(0),\ldots,Q(0),Q(W_{\Delta t})\} \in \mathbb{R}^{4(N+1)\times 4(N+1)}$, $\mathbf{P} = [P,\ldots,P] \in \mathbb{R}^{1\times 4(N+1)}$ are stacked vectors of Q and P in (25). Recall the $W_{\Delta t}(\neq 0)$ weight is only imposed in the terminal cost as described after (22).

Next, a new auxiliary variable, $\bar{\gamma}$, is introduced to represent the upper bound of stacked objective functions $\mathbf{J}$ such that

$$\mathbf{J} - \bar{\gamma} \le 0, \qquad \forall \mathbf{d} : \underline{\mathbf{d}} \le \mathbf{d} \le \bar{\mathbf{d}}. \tag{33}$$

Furthermore, we use an SDPR procedure to turn (33) into a semi-definite program and a Schur complement to eliminate involved nonlinearity when substituting (31) for $\mathbf{z}$ in $\mathbf{J}$, such that $\mathbf{J}-\bar{\gamma}$ can be written as

$$\mathbf{J} - \bar{\gamma} = -(\mathbf{d}-\underline{\mathbf{d}})^\top D(\bar{\mathbf{d}}-\mathbf{d}) - \begin{bmatrix}\mathbf{d}^\top & 1\end{bmatrix} L(\mathbf{u},D,\bar{\gamma}) \begin{bmatrix}\mathbf{d}\\ 1\end{bmatrix}, \tag{34}$$

where $D \succeq 0$ with $D \in \mathbb{D}^{2N}$ is a positive semi-definite diagonal matrix. $L(\mathbf{u},D,\bar{\gamma})$ is a linearised matrix dependent on $\mathbf{u}$, D, and $\bar{\gamma}$ as

$$L(\mathbf{u},D,\bar{\gamma}) = \begin{bmatrix} -\widetilde{D}_{zd}^\top \mathbf{Q}^\top \mathbf{Q}\widetilde{D}_{zd} + D & -D(\underline{\mathbf{d}}+\bar{\mathbf{d}})/2 - bd & 0 \\ * & \underline{\mathbf{d}}^\top D\bar{\mathbf{d}} - cd + \bar{\gamma} & \mathbf{u}^\top \widetilde{D}_{zu}^\top \mathbf{Q}^\top \\ * & * & I^{4(N+1)} \end{bmatrix}, \tag{35}$$

with $*$ denoting the symmetry element of the corresponding matrix, bd and cd are expressions of stacked matrices and vectors shown in (31). (See [34], [36] for detailed expressions.) An inspection of (34) verifies that (33) is satisfied if $D \succeq 0$ with $D \in \mathbb{D}^{2N}$ and if it satisfies the following LMI

$$L(\mathbf{u},D,\bar{\gamma}) \succeq 0. \tag{36}$$

In view of (30), the stacked inequality constraints $\underline{\mathbf{f}} \le \mathbf{f} \le \bar{\mathbf{f}}$ can be expanded as

$$\underline{\mathbf{f}} \le \widetilde{C}_f x(0) + \widetilde{D}_{fu}\mathbf{u} + \widetilde{D}_{fc}\mathbf{C} + \widetilde{D}_{fd}\mathbf{d} \le \bar{\mathbf{f}}, \tag{37}$$

which normally requires $3(N+1)$ LMI constraints for the upper and lower boundaries, respectively [34]. To reduce the computational burden, the sLMI approach which combines all $6(N+1)$ LMIs in (37) into a single LMI is presented next. First, (37) is written as

$$\begin{bmatrix} I^{3(N+1)} \\ -I^{3(N+1)} \end{bmatrix} \mathbf{f} \le \begin{bmatrix} \bar{\mathbf{f}} \\ -\underline{\mathbf{f}} \end{bmatrix} =: \bar{\mathbf{f}}^*. \tag{38}$$

To simplify the notation, let $\mathbf{I}^* = \begin{bmatrix} I^{3(N+1)} \\ -I^{3(N+1)} \end{bmatrix}$. By defining a new variable $\tilde{\mathbf{f}} \in \mathbb{R}^{6(N+1)}$, it is desirable to satisfy the single condition

$$\tilde{\mathbf{f}} := \bar{\mathbf{f}}^* - \mathbf{I}^*\mathbf{f} \ge 0, \tag{39}$$

such that constraints (37) are satisfied. From Theorem 3 of [36], let $e \in \mathbb{R}^{6(N+1)}$ be the vector of ones, then $\tilde{\mathbf{f}} \ge 0$ if there exist $\mu \in \mathbb{R}$ and $M \in \mathbb{D}^{6(N+1)}$ such that

$$\mathscr{L} = \begin{bmatrix} 2\mu & (\tilde{\mathbf{f}} - Me - e\mu)^\top \\ * & M + M^\top \end{bmatrix} \succeq 0. \tag{40}$$

By substituting (39) for $\tilde{\mathbf{f}}$ and (30) for $\mathbf{f}$ into (40), yields

$$\begin{bmatrix} 2\mu & \left(\bar{\mathbf{f}}^* - \mathbf{I}^*\left(\widetilde{C}_f x(0) + \widetilde{D}_{fu}\mathbf{u} + \widetilde{D}_{fc}\mathbf{C} + \widetilde{D}_{fd}\mathbf{d}\right) - (Me + e\mu)\right)^\top \\ * & M + M^\top \end{bmatrix} \succeq 0. \tag{41}$$

Applying the Schur complement to transform the left-hand-side of (41) into a scalar and followed by an SDPR procedure to remove the disturbance term $\mathbf{d}$, one can obtain a nonlinear matrix inequality constraint

$$L_{sLMI}(\tilde{D},\mu,M,\mathbf{u}) \succeq 0, \tag{42}$$

where $0 \preceq \tilde{D} \in \mathbb{D}^{2N}$ is a new slack variable. To remove the nonlinearity included, the Schur complement is applied again such that a linear $L_{sLMI}(\tilde{D},\mu,M,\mathbf{u})$ is determined as

$$L_{sLMI}(\tilde{D},\mu,M,\mathbf{u}) = \begin{bmatrix} \tilde{D} & -\tilde{D}(\bar{\mathbf{d}}+\underline{\mathbf{d}})/2 & \widetilde{D}_{fd}^\top \mathbf{I}^{*\top} \\ * & 2\mu + \underline{\mathbf{d}}^\top \tilde{D}\bar{\mathbf{d}} & \left(-\bar{\mathbf{f}}^* + \mathbf{I}^*\left(\widetilde{C}_f x(0) + \widetilde{D}_{fc}\mathbf{C} + \widetilde{D}_{fu}\mathbf{u}\right) + (Me + e\mu)\right)^\top \\ * & * & \left(M + M^\top\right) \end{bmatrix}. \tag{43}$$

Remark 1: Detailed derivation steps from LMI (41) to matrix (43) can be referred to Appendix A.

Therefore, if the single LMI (42) of (43) is satisfied, all constraints in (37) are satisfied.

To summarise, the RMPC formulation of the optimisation problem under the space-domain scheme, after applying SDPR, Schur complement and sLMI, can be organised as

$$\min_{\mathbf{u}} \quad \bar{\gamma}, \tag{44a}$$

$$\textbf{s.t.} \quad L(\mathbf{u},D,\bar{\gamma}) \succeq 0, \tag{44b}$$

$$L_{sLMI}(\tilde{D},\mu,M,\mathbf{u}) \succeq 0, \tag{44c}$$

$$\begin{bmatrix} \zeta(0) \\ \zeta(1) \\ \vdots \\ \zeta(N-1) \end{bmatrix} \ge \begin{bmatrix} 1/\sqrt{2E(0)/m} \\ 1/\sqrt{2E(1)/m} \\ \vdots \\ 1/\sqrt{2E(N-1)/m} \end{bmatrix}, \tag{44d}$$

$$\textbf{given:} \quad x(0) = [E(0), \Delta t(0)]^\top, \tag{44e}$$

$$0 \preceq D \in \mathbb{D}^{2N}, \tag{44f}$$

$$0 \preceq \tilde{D} \in \mathbb{D}^{2N}. \tag{44g}$$

Remark 2: The recursive feasibility of the proposed scheme could be potentially guaranteed by utilising the standard shifting arguments and the assumption that the invariant terminal set is defined by the terminal constraint. In particular,

the optimal control sequence $(\{u(k \mid k), u(k+1 \mid k), u(k+2 \mid k), \ldots, u(k+N-1 \mid k)\})$ computed at sample k can be shifted and appended with an extra terminal control law $u(k+N)$ obtained by imposing an invariant set of the terminal constraints to yield the control sequence $\{u(k+1 \mid k), u(k+2 \mid k), \ldots, u(k+N-1 \mid k), u(k+N)\}$ which remains feasible at the next sample $k+1$. For more details refer to [36], [49], [50]. On the other hand, a series of numerical simulations have been carried out to illustrate that the proposed REACC scheme can provide recursively feasible solutions through trial and error. Nevertheless, further rigorous investigation into recursive feasibility has been scheduled for future work.

B. Nominal MPC for benchmarking

In this subsection, a nominal (disturbance-free) MPC is introduced, which will be utilised as a benchmark and compared with the proposed REACC scheme in Section V-B. Since the nominal MPC does not involve disturbances in its dynamic state-space equations, $d(k)$ as well as the associated condensed form $\mathbf{d}$ are set to zero. Based on the original convex OCP organised in (21) with $d(k)$ eliminated, and eliminating $\mathbf{d}$ terms in (29), (30), and (31), a condensed nominal MPC formulation can be summarised as

$$\min_{\mathbf{u}} \quad \check{\mathbf{J}} = (\check{\mathbf{z}} - \bar{\mathbf{z}})^{\top} \mathbf{Q}^{\top} \mathbf{Q} (\check{\mathbf{z}} - \bar{\mathbf{z}}) + \mathbf{P}\check{\mathbf{z}} + \check{\mathbf{z}}^{\top} \mathbf{P}^{\top}, \tag{45a}$$

$$\text{s.t. } \check{\mathbf{x}} = \widetilde{A}\check{x}(0) + \widetilde{B}_u \mathbf{u} + \widetilde{B}_c \mathbf{C}, \tag{45b}$$

$$\check{\mathbf{f}} = \widetilde{C}_f \check{x}(0) + \widetilde{D}_{fu} \mathbf{u} + \widetilde{D}_{fc} \mathbf{C}, \tag{45c}$$

$$\check{\mathbf{z}} = \widetilde{C}_z \check{x}(0) + \widetilde{D}_{zu} \mathbf{u} + \widetilde{D}_{zc} \mathbf{C}, \tag{45d}$$

$$\underline{\mathbf{f}} \leq \check{\mathbf{f}} \leq \bar{\mathbf{f}}, \tag{45e}$$

$$\begin{bmatrix} \zeta(0) \\ \zeta(1) \\ \vdots \\ \zeta(N-1) \end{bmatrix} \geq \begin{bmatrix} 1/\sqrt{2\check{E}(0)/m} \\ 1/\sqrt{2\check{E}(1)/m} \\ \vdots \\ 1/\sqrt{2\check{E}(N-1)/m} \end{bmatrix}, \tag{45f}$$

$$\text{given: } \check{x}(0) = [E(0), \Delta t(0)]^{\top}. \tag{45g}$$

where the variables $\check{E}(k)$, $\check{x}(0)$, $\check{\mathbf{J}}$, $\check{\mathbf{x}}$, $\check{\mathbf{f}}$, and $\check{\mathbf{z}}$ have the same meaning as the already introduced variables $E(k)$, $x(0)$, $\mathbf{J}$, $\mathbf{x}$, $\mathbf{f}$, and $\mathbf{z}$, respectively, but have different evolution because they are not affected by disturbances.

V. Simulation Results

The evaluation of the proposed space-domain REACC method is fourfold: 1) the robustness of the RMPC method is investigated and compared with a nominal benchmark MPC method (described in Section IV-B) given the same initial conditions and disturbances in simulations; 2) a comprehensive comparison is conducted between space-domain (denoted by REACC) and time-domain formulations described in [35] in terms of energy consumption and passenger comfort using the same RMPC method in both domains under identical initial conditions and disturbances; 3) the proposed REACC is further compared with a benchmark method using a CDFS that targets a fixed inter-vehicular distance gap in terms of energy efficiency; 4) the computational efficiency of the sLMI-based REACC method is examined by evaluating the average running time required for each iteration. The numerical simulations are tested in the Matlab environment using the optimisation toolbox Yalmip [51] with MOSEK solver [52] on a 2.3 GHz quad-core Intel Core i5 with an 8 GB of 2133 MHz LPDDR3 onboard memory. Before presenting the numerical examples, the velocity profiles of the leading vehicle and the definition of the disturbances are given.

A. Simulation setup

The leading vehicle in the following simulations is operated on an experimental route, of which the data is collected on a real-world route in London UK as shown in Fig. 5. The road profile data and the traffic constraint of the selected test route are collected based on *Google Maps* and are shown in Fig. 6, which includes a plot on the road curvature profile (top subplot), a plot on the leading vehicle velocity, its prediction, and the combined speed limit (middle subplot), and a plot on the road slope angle (bottom subplot).

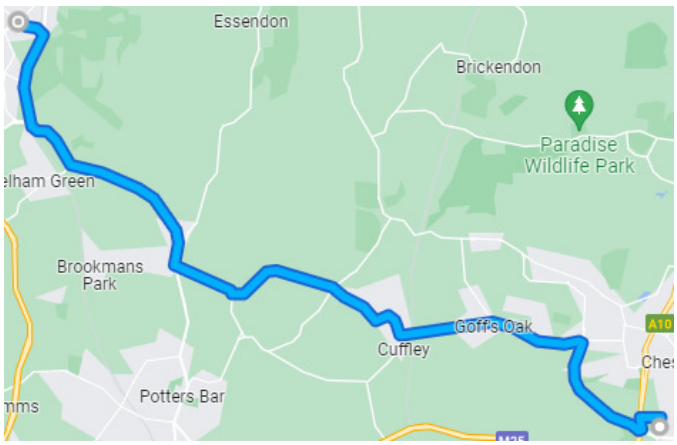

Fig. 5: 18.7 km route in London UK selected for the velocity profile of the leading vehicle in the numerical simulations. (https://goo.gl/maps/2CTCW7smdCkGCsKv5)

Specifically, the top subplot of Fig. 6 shows the actual curvature κ of the test route. The middle subplot contains three velocity profiles represented by different colours. The yellow curve denotes the combined speed limit of this selected route, $v_{\max}(v_{leg}, \kappa)$, which is dependent on the legal speed limit as well as the cornering speed limit which is further dependent on the road curvature (calculated by (8)). The blue trajectory represents the actual velocity profile of the leading vehicle (i.e., v_l), which follows an experimental velocity profile collected by a human-driven passenger car on the real route. It can be observed that this non-optimised velocity profile could involve aggressive manoeuvres (e.g., at s=4.6 km) and violations of the speed limit (e.g., at s=12 km). Moreover, we introduce the red curve ($v_{l,f}$) that is obtained by passing the real velocity profile (the blue curve) through a low-pass filter to remove sharp changes in speed, which can be understood as unexpected events and high-frequency noises from communication or sensing. Furthermore, the filtered speed profile is capped by

This article has been accepted for publication in IEEE Transactions on Transportation Electrification. This is the author's version which has not been fully edited and content may change prior to final publication. Citation information: DOI 10.1109/TTE.2023.3340670

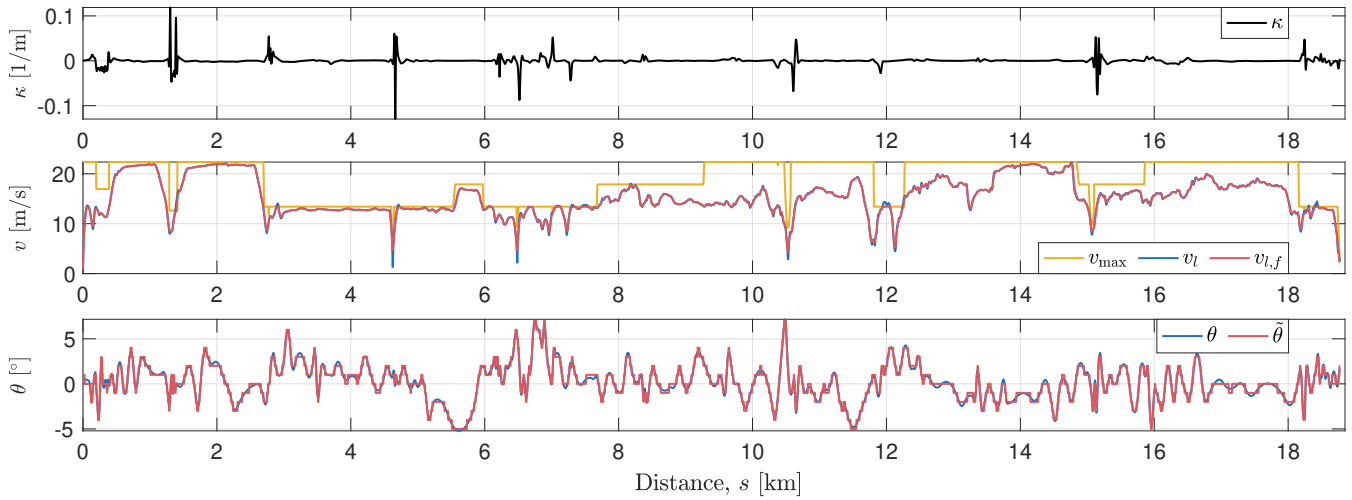

Fig. 6: Detailed road information of the London UK route with: a) actual road curvature (top), b) actual leading vehicle velocity v_l, 'filtered' leading vehicle velocity $v_{l,f}$, and combined speed limit $v_{\max}$ (middle), and c) actual and nominal road slope angles, θ and $\tilde{\theta}$, respectively (bottom).

the legal speed limit. Let us now recall the background of the EACC problem that the ego vehicle has access to a future velocity profile of the leading vehicle through V2V/V2I communication. Unlike simulation setups in other literature that further embed data- or learning-based velocity predictors [12] or conservatively assume the leading vehicle maintains the current acceleration [17], this work adopts the velocity profile of $v_{l,f}$ as the future velocity plan such that the prediction of the leading vehicle $\tilde{v}_l(k{:}k{+}N{-}1)$ available to the ego vehicle is generated by setting $\tilde{v}_l(k{:}k{+}N{-}1){=}v_{l,f}(k{:}k{+}N{-}1)$, $\forall k \in [0, k_s]$). This setup practically fits into the framework of the connected EACC scenario, where the shared future velocity profile is a smooth and legal plan while the actual velocity profile contains some non-optimal and even illegal driving behaviours. The accuracy of the predicted leading velocity profile against the actual velocity profile in this work is similar to the present vehicle velocity prediction ability [53]. To this end, the implementation of MPC demanding the prediction of Δt (by (14)) within the control horizon, which in turn requires a prediction of the leading vehicle velocity, $\tilde{v}_l$, is completed. The resulting velocity error between the actual and predicted profiles further results in the disturbance on the time gap state, d_t, (determined by (27)).

The bottom subplot of Fig. 6 illustrates the slope angle profiles of the road, where the blue curve denotes the actual road slope angle trajectory θ collected from the latest *Google Maps* database, with $\theta(k) \in [\underline{\theta}, \overline{\theta}]$. The nominal (available to the ego vehicle) slope angle profile, $\tilde{\theta}$ (red curve in the same subplot), is obtained after rounding θ to integers in degrees. The difference between the actual and nominal slope angle leads to the associated modelling mismatch $\Delta\theta$ in (2).

In addition to the modelling mismatch on the road slope angle as well as the communication or the sensing error on the velocity of the leading vehicle, the disturbances considered in this work also come from modelling mismatches on the air-drag and the tyre-rolling resistance coefficients. The practical air-drag resistance coefficients utilised in this work

TABLE II: VEHICLE PARAMETERS AND ROAD CHARACTERISTICS.

Descriptions	Symbols	Values
Acceleration of gravity	g	9.81 m/s^2
Ego vehicle mass	m	1200 kg
Nominal air-drag coefficient	$\tilde{f}_d$	0.34 kg/m
Nominal tyre-rolling resistance coefficient	$\tilde{f}_r$	0.01
Ego vehicle initial velocity	v_0	0.9108 m/s
Initial time gap	$\Delta t(0)$	3 s
Acceleration limits	$a_{x,max}/a_{y,max}$	9.81 m/s^2
Min velocity limit	$v_{\min}$	0.1 m/s
Min/max time gap	$\Delta t_{\min}/\Delta t_{\max}$	1/8 s
Limits of air-drag coefficient	$\underline{f}_d/\overline{f}_d$	0.296/0.380 kg/m
Limits of tyre-rolling resistance coefficient	$\underline{f}_r/\overline{f}_r$	0.008/0.012
Limits of road slope	$\underline{\theta}/\overline{\theta}$	$-5.22°/7.17°$
Limits of road slope mismatch	$\underline{\Delta\theta}/\overline{\Delta\theta}$	$-0.5°/0.5°$
Limits of disturbance on kinetic energy	$\underline{d}_E/\overline{d}_E$	$-146.28/148.20$ N
Limits of disturbance on time gap	$\underline{d}_t/\overline{d}_t$	$-0.58/0.11$ s/m

are obtained according to a fitted look-up table associated with the real-time inter-vehicular distance gap [44], which are also used to provide $\underline{f}_d$ and $\overline{f}_d$. The actual tyre-rolling resistance coefficients adopted in the simulations are randomly generated within the specified realistic bounds of the coefficient, $\underline{f}_r$ and $\overline{f}_r$, with a uniform distribution. The nominal coefficients of the air-drag and tyre-rolling resistance, $\tilde{f}_d$ and $\tilde{f}_r$ respectively, are determined by the middle points of the associated bounds. Furthermore, the overall disturbance on the ego vehicle kinetic energy d_E and its limits are obtained by merging all modelling mismatches on f_d, f_r, and θ, and their limits, respectively, by (26), with $d_E(k) \in [\underline{d}_E, \overline{d}_E]$. Additionally, the sampling distance interval is set to $\delta s{=}3$ m.

The limits of disturbances discussed as well as other main characteristic parameters of the ego vehicle model are summarised in Table. II.

B. Comparisons between nominal MPC and RMPC

A comparison of the ego vehicle speed trajectories between the REACC proposed in (44) and the nominal MPC benchmark formulated in (45) is illustrated in Fig. 7. After simulating with identical disturbances in both the nominal MPC benchmark as well as the proposed REACC scheme, it can be observed that when the travelled distance reaches 4.617 km in the zoomed-in box of Fig. 7, the velocity trajectory of the nominal MPC violates the speed limit constraint, which leads to infeasible solutions. In contrast, the robust controller (REACC) can always satisfy the velocity constraint with feasible solutions, which verifies the robustness of the RMPC.

Furthermore, it is worth noticing that the behaviours of both nominal and robust MPC algorithms are similar to each other in most of the travelled distance. However, close to the position where the nominal scheme becomes infeasible (e.g., $s = 4.617$ km), the resulting velocity trajectory of the REACC starts to differ from the velocity profile generated by the benchmark nominal MPC. This is understood that the REACC scheme determines state constraints based on disturbance boundaries as well as the current state in a real-time manner. When the velocity and other constraints are not tight, the REACC provides control solutions similar to nominal MPC which does not consider disturbances. On the other hand, when the velocity constraint is tight, due to the real-time constraint boundary calculation, the RMPC provides solutions that are different from solutions of nominal MPC to ensure feasibility, at the cost of some degree of optimality.

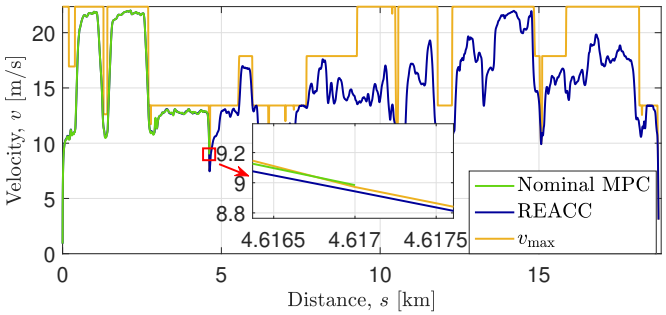

Fig. 7: A comparison of the ego vehicle speed trajectories between the REACC method and the nominal MPC under the same initial conditions and simulation disturbances.

C. Comparison between time- and space-domain schemes

In this section, the energy saving and driving performances of the space-domain formulation are investigated by comparing the proposed space-domain formulated REACC scheme against the results yielded by a benchmark scheme using the same proposed RMPC but formulated in the time-domain. The benchmark scheme utilises the feedback linearisation method to linearise the vehicle dynamic motion [19] as well as an energy consumption model based on the L^2 norm of the acceleration [35], under the same initial conditions, constraints, exogenous input (leading vehicle velocity), and disturbances. To further ensure the fairness of the comparison, the sampling interval of the time-domain scheme is chosen as 0.2 s, which guarantees the equivalence of the sampling interval as well as the total number of samples of the two domain schemes, based on the average velocity of the profiles generated by the two schemes. In addition, the weighting parameters are selected carefully such that the most optimal performance in terms of energy consumption is provided by each scheme, respectively. Moreover, the weights in the cost functions of both time- and space-domain MPC schemes are finely adjusted for a small number of iterations at the end of the simulation to ensure negligible differences in terms of the terminal speed (the terminal speeds of the ego vehicles in both domains and the final speed of the leading vehicle are all the same). As such, the involvement of the kinetic energy change can be excluded and the total energy consumption during a driving cycle can be directly compared as the battery energy usage, $E_b = \sum_{k=0}^{k_s-1} P_b(F_t^*(k), v^*(k)) \frac{\delta s}{v^*(k)}$, which is a part of the original multi-objective cost function in (12). $F_t^*(k)$ is the optimal input force on the wheels and $v^*(k)$ is the optimal speed determined by the utilised control methods. To this end, with the aforementioned arrangements excluding other possible interference, the intended comparisons of electric battery powertrain energy consumption as well as driving behaviours between the space- and time-domain formulations can be carried out with ensured fairness.

In Fig. 8, the comparison of the battery energy consumption of the space-domain (denoted by REACC) and the time-domain RMPC schemes is presented. As it can be seen for all cases in Fig. 8, the REACC scheme can save around 4.8% battery energy consumption as compared with the results of the time-domain formulated benchmark. Moreover, the largest improvement of roughly 5% can be found when the prediction horizon is 17. In addition, the average velocity of the REACC is found to be higher than that of the benchmark by 7.33%, which shows the superiority of the REACC in both objectives of maximising mobility and saving energy.

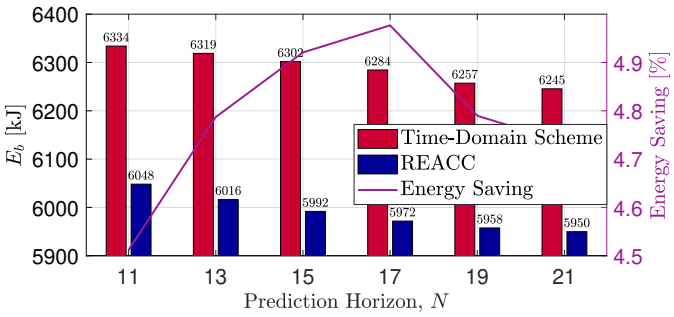

Fig. 8: Comparisons of the battery energy consumption (E_b) of the proposed REACC and time-domain RMPC schemes, for different prediction horizon lengths.

Further investigation of the driving comfort verifies the finding of the energy saving superiority of the REACC strategy. As shown in Fig. 9, the driving comfort is evaluated by the root-mean-square (RMS) of acceleration and jerk $\left(j = \frac{d^2v}{dt^2}\right)$ of the ego vehicle [54]. The proposed REACC method achieves lower values of both indexes against the time-domain benchmark for all prediction horizon length choices. The findings in

This article has been accepted for publication in IEEE Transactions on Transportation Electrification. This is the author's version which has not been fully edited and content may change prior to final publication. Citation information: DOI 10.1109/TTE.2023.3340670

both Fig. 8 and Fig. 9 can be understood that as compared to the time-domain formulated benchmark method, the REACC strategy, in addition to the highly accurate and convexified powertrain fitting model embedded into the cost function, which is exclusively enabled in the space-domain formulation, tends to avoid large accelerations and achieve a smooth driving profile, hence it is expected to be more energy efficient in terms of powertrain operation.

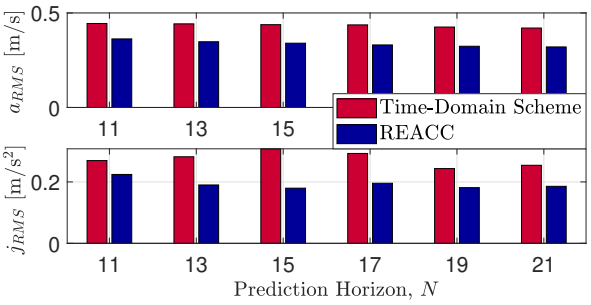

Fig. 9: Comparisons of the RMS acceleration and RMS jerk throughout the mission of the proposed REACC and time-domain RMPC schemes, for different prediction horizon lengths.

To provide further insight into the comparison of the two schemes, analyses of the ego vehicle velocity profile and inter-vehicular gap have been provided in Fig. 10 and Fig. 11, respectively, for the case of prediction horizon $N = 11$. Fig. 10 shows that although the time-domain scheme with L^2 norm of the acceleration in its objective function directly penalises magnitudes of accelerations, its associated velocity profile contains more frequent velocity changes compared to the REACC scheme that does not directly minimise the acceleration magnitude, which is aligned with the result in Fig. 9. This is understood that, compared with the space-domain formulation where the weights of two objectives in the cost function are more balanced, a relatively heavier weight is applied to the objective of following the speed limit in the time-domain formulation while a lighter weight is applied to the L^2 norm of the acceleration (which is directly related to energy consumption and velocity profile smoothness). As shown by Fig. 11, the time-domain scheme is more likely to push the ego vehicle to approach the minimum time gap (Δt) constraint. Since the current weighting in the time-domain scheme is unbalanced, one may suggest further increasing the weight on the L^2 norm of the acceleration. Although this suggestion may help to save energy, smooth the velocity profile, and hence improve comfort, it also makes the velocity profile less varying and therefore less able to maintain the Δt within the gap constraints as the leading vehicle velocity changes frequently. On the other hand, since the objective function of the space-domain formulation utilises a fitted quadratic function of driving force for the energy consumption, minimising energy consumption does not directly penalise the change of velocity. Therefore, its velocity profile is more flexible (observe in Fig. 11 that the blue curve fully makes use of the allowed range) and the scheme can bear a heavier weight on energy consumption penalisation.

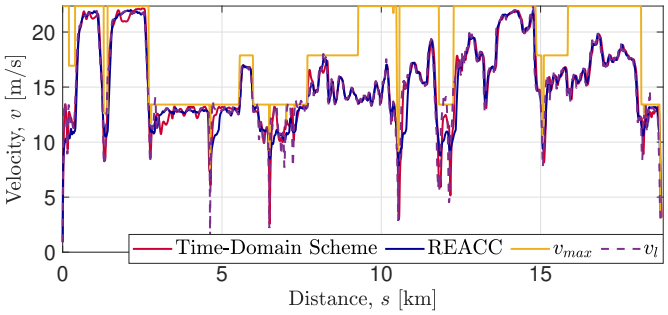

Fig. 10: A comparison of the ego vehicle velocity (v) of the proposed REACC and time-domain RMPC schemes, taking the prediction horizon length $N = 11$ as an example.

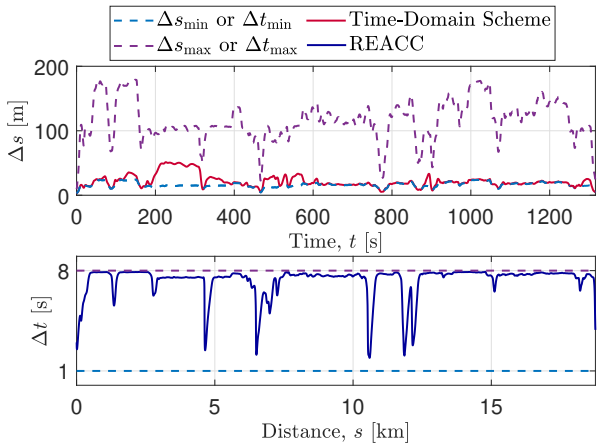

Fig. 11: A comparison of the inter-vehicular distance gap (Δs) by the time-domain RMPC scheme and the time gap (Δt) by the proposed REACC, taking the prediction horizon length $N = 11$ as an example.

D. Comparison between CDFS and proposed REACC schemes

This section investigates the energy economy of the proposed REACC against a benchmark using a CDFS scheme by which the velocity of the ego vehicle is identical to that of the leading vehicle. The powertrain operating points of the ego vehicles for the two methods are evaluated based on the battery electric vehicle powertrain efficiency map (Fig. 3b). As shown in Fig. 12, the operating points of the CDFS are widely allocated with more points being found closer to the operational boundaries (red dash rectangle), which are less efficient regions. As for the REACC, the operating points are more concentrated and mostly located within the highly efficient zone. Therefore, the REACC method can drive the vehicle in a more ecological way compared to the CDFS, yielding 11.53% (N=11 of REACC) of energy saving.

Furthermore, the composition of various energy losses is presented in Fig. 13. Although the two schemes have similar amounts of air-drag and tyre-rolling resistance losses (illustrated by heights of the orange and blue bars, respectively), the proposed REACC can reduce up to 40.1% and 18.6% the energy losses caused by powertrain regeneration and propulsion, respectively. Moreover, the mechanical braking is completely avoided when REACC is deployed, while it contributes to approximately 0.369% of the losses in the case of the CDFS (not shown in Fig. 13), which reinforces the

This article has been accepted for publication in IEEE Transactions on Transportation Electrification. This is the author's version which has not been fully edited and content may change prior to final publication. Citation information: DOI 10.1109/TTE.2023.3340670

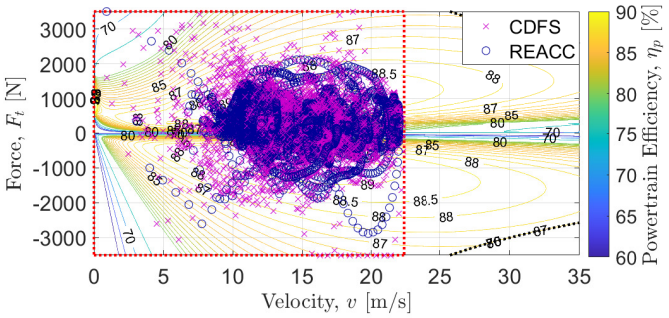

Fig. 12: Operating points of REACC (N=11) and CDFS schemes.

validity of the choice of (20) as the OCP cost function, in which F_t is replaced by F_w. As a result, the total powertrain loss (propulsion and regeneration) of REACC can be reduced by up to 23.43% as compared to the CDFS scheme. Note that the change of kinetic energy corresponding to the difference between the initial and the final velocities of the ego vehicle, as well as the potential energy change because of the height differences between the initial and final positions of the ego vehicle are identical, respectively, in simulations with both the CDFS and REACC schemes due to the terminal speed condition imposed to the REACC scheme (similarly to Section V-C) and the equal travelled distance of the two schemes. Therefore, these quantities are not included in the energy loss comparison between the two schemes. These findings further verify the finding in Fig. 12 of the capability of the REACC to achieve a more ecological driving behaviour.

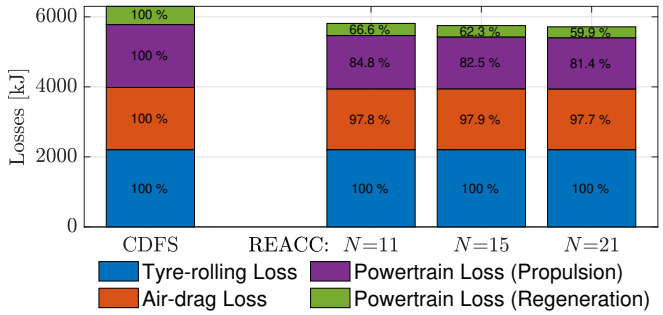

Fig. 13: Energy loss compositions breakdown by REACC (N=11,15,21) and CDFS schemes, for different prediction horizon lengths. Energy losses are categorised into four main types: tyre-rolling, air-drag, powertrain propulsion, and powertrain regeneration losses. Each type of loss is represented by a different colour and is labelled by a number that shows the relative quantity of the loss by REACC compared to the same type of loss by CDFS in terms of percentage. Although a portion of consumed energy can also be dissipated through mechanical braking, this type of loss is not included in the figure since its amount compared with other loss types is negligible. Specifically, mechanical braking amounts to 0.369% of total losses for the CDFS scheme, while the REACC schemes can fully avoid mechanical braking losses.

E. Verification of the approach in real-time implementation

The computational burden of the proposed REACC is evaluated in this part. The test results are presented in Fig. 14. The average computational time required for each iteration can be reduced to 0.141 s when N=11. When the prediction horizon is enlarged, the computational cost monotonically increases and reaches 0.463 s when N=21. Given the fixed sampling distance interval, δs=3 m, and the average velocity (15.22 m/s) of following this experimental drive cycle, which would result in an average sampling time interval of 0.21 s, the result shows a possibility of implementing the REACC scheme in real-time. One of the key contributors to saving computation time is the sLMI technique, which is able to compact multiple LMIs into a single LMI rather than process LMIs individually as an mLMI technique. To further justify the claim, the computational efficiencies of the REACC scheme are compared in Fig. 14 with those of another identical RMPC-based EACC scheme as the proposed one but which utilises the previously developed mLMI instead of the proposed sLMI technique. The figure demonstrates that for various prediction horizon length choices in comparison to the mLMI-based method the REACC can reduce the computational time from 17% up to approximately 48%, while, the accumulated optimisation objective $\overline{\gamma}$ in (44a) over the whole car-following task is sacrificed by a negligible amount (0.0092%) in an example case where $N = 11$.

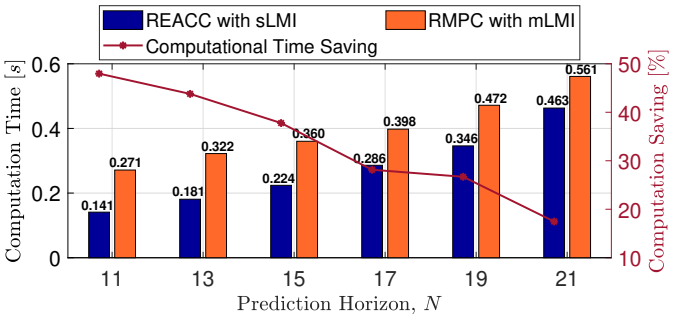

Fig. 14: Comparisons between mean computation time per iteration for different prediction horizon lengths by REACC with the sLMI scheme and RMPC with mLMI.

VI. Conclusions

In this work, the REACC problem is addressed by proposing a robust convex energy-optimal adaptive cruise control strategy. To deal with the disturbances dominated by modelling mismatches, an RMPC controller with SDPR and sLMI constraint formulation is designed to enhance the robustness of the system as well as address the computational issue. By applying conservative relaxation and convexification on the battery electric vehicle powertrain and the system dynamics, the overall REACC problem is formulated as a convex optimisation problem in the space-domain. The performance of the proposed REACC is evaluated on a real-world London UK driving cycle against three benchmarks under the same initial conditions and simulation disturbances. The robustness of the REACC is verified through the comparison with the infeasible solutions yielded by a nominal-based MPC. As compared to a benchmark RMPC in the time-domain, the REACC method

in space-domain is able to achieve a 4.5% $\sim$ 5% higher energy efficiency thanks to a precisely fitted battery powertrain model, as well as an improved driving comfort with less jerky manoeuvres, which further contributes to energy-saving. Moreover, the REACC scheme is compared with a CDFS scheme by investigating energy economy, powertrain operating points and energy loss compositions, and it is found to reduce energy losses by approximately 11%, which further illustrates the contribution towards energy saving by the REACC strategy. By further investigating computational time, it is verified that the REACC can be potentially implemented in real-time with enhanced energy economy, driving comfort and robustly satisfied safety constraints without sacrificing optimality.

Future work could involve a further hardware-in-the-loop investigation of the performance and computational benefits of the proposed space-domain scheme in further realistic and more demanding driving missions as well as with consideration of practical powertrain characteristics, such as thermal effects. On the other hand, a rigorous proof and analysis of the recursive feasibility of the presented methodology can also be addressed, as well as a comparison of the performance of new implementations of other robust approaches in the EACC problem, such as with the Tube-MPC.

APPENDIX A

Recall the LMI in (41)

$$\begin{bmatrix} 2\mu & \left(\bar{\mathbf{f}}^*-\mathbf{I}^*\left(\widetilde{C}_f x(0)+\widetilde{D}_{fu}\mathbf{u}+\widetilde{D}_{fc}\mathbf{C}+\widetilde{D}_{fd}\mathbf{d}\right)-(Me+e\mu)\right)^\top \\ * & M+M^\top \end{bmatrix} \succeq 0.$$

Applying the Schur complement to transform the left-hand-side of (41) into a scalar

$$\begin{aligned}
&=2\mu- \\
&\quad \left(\bar{\mathbf{f}}^*-\mathbf{I}^*\left(\widetilde{C}_f x(0)+\widetilde{D}_{fu}\mathbf{u}+\widetilde{D}_{fc}\mathbf{C}+\widetilde{D}_{fd}\mathbf{d}\right)-(Me+e\mu)\right)^\top \cdot \\
&\quad \left(M+M^\top\right)^{-1} \cdot \\
&\quad \left(\bar{\mathbf{f}}^*-\mathbf{I}^*\left(\widetilde{C}_f x(0)+\widetilde{D}_{fu}\mathbf{u}+\widetilde{D}_{fc}\mathbf{C}+\widetilde{D}_{fd}\mathbf{d}\right)-(Me+e\mu)\right) \\
&=2\mu- \\
&\quad \left(\bar{\mathbf{f}}^{*\top}-x(0)^\top\widetilde{C}_f^\top\mathbf{I}^{*\top}-\mathbf{u}^\top\widetilde{D}_{fu}^\top\mathbf{I}^{*\top}-\mathbf{C}^\top\widetilde{D}_{fc}^\top\mathbf{I}^{*\top}-\mathbf{d}^\top\widetilde{D}_{fd}^\top\mathbf{I}^{*\top}-(Me+e\mu)^\top\right) \cdot \\
&\quad \left(M+M^\top\right)^{-1} \cdot \\
&\quad \left(\bar{\mathbf{f}}^*-\mathbf{I}^*\widetilde{C}_f x(0)-\mathbf{I}^*\widetilde{D}_{fu}\mathbf{u}-\mathbf{I}^*\widetilde{D}_{fc}\mathbf{C}-\mathbf{I}^*\widetilde{D}_{fd}\mathbf{d}-(Me+e\mu)\right).
\end{aligned}$$

Since $\bar{\mathbf{f}}^*$, $\mathbf{I}^*\widetilde{C}_f x(0)$, and $\mathbf{I}^*\widetilde{D}_{fc}\mathbf{C}$ are all constant terms, by defining a new $\bar{\mathbf{f}}' = \bar{\mathbf{f}}^* - \mathbf{I}^*\widetilde{C}_f x(0) - \mathbf{I}^*\widetilde{D}_{fc}\mathbf{C}$, the scalar can be further simplified as in

$$\begin{aligned}
&=2\mu - \left(\bar{\mathbf{f}}'^\top-\mathbf{u}^\top\widetilde{D}_{fu}^\top\mathbf{I}^{*\top}-\mathbf{d}^\top\widetilde{D}_{fd}^\top\mathbf{I}^{*\top}-(Me+e\mu)^\top\right) \cdot \\
&\quad \left(M+M^\top\right)^{-1}\left(\bar{\mathbf{f}}'-\mathbf{I}^*\widetilde{D}_{fu}\mathbf{u}-\mathbf{I}^*\widetilde{D}_{fd}\mathbf{d}-(Me+e\mu)\right) \\
&=2\mu-\bar{\mathbf{f}}'^\top\left(M+M^\top\right)^{-1}\bar{\mathbf{f}}'+\bar{\mathbf{f}}'^\top\left(M+M^\top\right)^{-1}\mathbf{I}^*\widetilde{D}_{fu}\mathbf{u}+ \\
&\quad \bar{\mathbf{f}}'^\top\left(M+M^\top\right)^{-1}\mathbf{I}^*\widetilde{D}_{fd}\mathbf{d}+\bar{\mathbf{f}}'^\top\left(M+M^\top\right)^{-1}(Me+e\mu)+ \\
&\quad \mathbf{u}^\top\widetilde{D}_{fu}^\top\mathbf{I}^{*\top}\left(M+M^\top\right)^{-1}\bar{\mathbf{f}}'-\mathbf{u}^\top\widetilde{D}_{fu}^\top\mathbf{I}^{*\top}\left(M+M^\top\right)^{-1}\mathbf{I}^*\widetilde{D}_{fu}\mathbf{u}- \\
&\quad \mathbf{u}^\top\widetilde{D}_{fu}^\top\mathbf{I}^{*\top}\left(M+M^\top\right)^{-1}\mathbf{I}^*\widetilde{D}_{fd}\mathbf{d}- \\
&\quad \mathbf{u}^\top\widetilde{D}_{fu}^\top\mathbf{I}^{*\top}\left(M+M^\top\right)^{-1}(Me+e\mu)+ \\
&\quad \mathbf{d}^\top\widetilde{D}_{fd}^\top\mathbf{I}^{*\top}\left(M+M^\top\right)^{-1}\bar{\mathbf{f}}'-\mathbf{d}^\top\widetilde{D}_{fd}^\top\mathbf{I}^{*\top}\left(M+M^\top\right)^{-1}\mathbf{I}^*\widetilde{D}_{fu}\mathbf{u}- \\
&\quad \mathbf{d}^\top\widetilde{D}_{fd}^\top\mathbf{I}^{*\top}\left(M+M^\top\right)^{-1}\mathbf{I}^*\widetilde{D}_{fd}\mathbf{d}- \\
&\quad \mathbf{d}^\top\widetilde{D}_{fd}^\top\mathbf{I}^{*\top}\left(M+M^\top\right)^{-1}(Me+e\mu)+ \\
&\quad (Me+e\mu)^\top\left(M+M^\top\right)^{-1}\bar{\mathbf{f}}'-(Me+e\mu)^\top\left(M+M^\top\right)^{-1}\mathbf{I}^*\widetilde{D}_{fu}\mathbf{u}- \\
&\quad (Me+e\mu)^\top\left(M+M^\top\right)^{-1}\mathbf{I}^*\widetilde{D}_{fd}\mathbf{d}- \\
&\quad (Me+e\mu)^\top\left(M+M^\top\right)^{-1}(Me+e\mu).
\end{aligned}$$

After applying the SDPR procedure to decouple terms with disturbance $\mathbf{d}$ and introducing a new variable, $0 \preceq \tilde{D} \in \mathbb{D}^{2N}$, the scalar is rewritten as

$$(\mathbf{d}-\underline{\mathbf{d}})^\top\tilde{D}(\overline{\mathbf{d}}-\mathbf{d})+\begin{bmatrix}\mathbf{d}^\top & 1\end{bmatrix}L_{sLMI}(\tilde{D},\mu,M,\mathbf{u})\begin{bmatrix}\mathbf{d}\\1\end{bmatrix},$$

where $L_{sLMI}(\tilde{D},\mu,M,\mathbf{u}) =$

$$\begin{bmatrix}\tilde{D} & -\tilde{D}(\overline{\mathbf{d}}+\underline{\mathbf{d}})/2 \\ * & 2\mu+\underline{\mathbf{d}}^\top\tilde{D}\overline{\mathbf{d}}\end{bmatrix} - \begin{bmatrix}\widetilde{D}_{fd}^\top\mathbf{I}^{*\top} \\ \left(-\bar{\mathbf{f}}'+\mathbf{I}^*\widetilde{D}_{fu}\mathbf{u}+(Me+e\mu)\right)^\top\end{bmatrix} \cdot \left(M+M^\top\right)^{-1}\begin{bmatrix}\mathbf{I}'\widetilde{D}_{fd} & -\bar{\mathbf{f}}'+\mathbf{I}^*\widetilde{D}_{fu}\mathbf{u}+(Me+e\mu)\end{bmatrix}.$$

Furthermore, the Schur complement is utilised here to eliminate nonlinear terms included in the matrix. Moreover, substituting back $\bar{\mathbf{f}}' = \bar{\mathbf{f}}^* - \mathbf{I}^*\widetilde{C}_f x(0) - \mathbf{I}^*\widetilde{D}_{fc}\mathbf{C}$, as written in (43), the matrix $L_{sLMI}(\tilde{D},\mu,M,\mathbf{u})$ is

$$L_{sLMI}(\tilde{D},\mu,M,\mathbf{u}) = \begin{bmatrix}\tilde{D} & -\tilde{D}(\overline{\mathbf{d}}+\underline{\mathbf{d}})/2 & \widetilde{D}_{fd}^\top\mathbf{I}^{*\top} \\ * & 2\mu+\underline{\mathbf{d}}^\top\tilde{D}\overline{\mathbf{d}} & \left(-\bar{\mathbf{f}}^*+\mathbf{I}^*\left(\widetilde{C}_f x(0)+\widetilde{D}_{fc}\mathbf{C}+\widetilde{D}_{fu}\mathbf{u}\right)+(Me+e\mu)\right)^\top \\ * & * & \left(M+M^\top\right)\end{bmatrix}.$$

Hence, (41) is held, if the LMI $L_{sLMI}(\tilde{D},\mu,M,\mathbf{u}) \succeq 0$ is true.

REFERENCES

[1] Q. Yuan, Y. Ye, Y. Tang, Y. Liu, and G. Strbac, "A novel deep-learning based surrogate modeling of stochastic electric vehicle traffic user equilibrium in low-carbon electricity–transportation nexus," *Applied Energy*, vol. 315, p. 118961, 2022.

[2] C. Zhang, F. Yang, X. Ke, Z. Liu, and C. Yuan, "Predictive modeling of energy consumption and greenhouse gas emissions from autonomous electric vehicle operations," *Applied Energy*, vol. 254, p. 113597, 2019.

[3] S. He, F. Ding, C. Lu, and Y. Qi, "Impact of connected and autonomous vehicle dedicated lane on the freeway traffic efficiency," *European Transport Research Review*, vol. 14, no. 1, p. 12, 2022.

[4] J. Guanetti, Y. Kim, and F. Borrelli, "Control of connected and automated vehicles: State of the art and future challenges," *Annual Reviews in Control*, vol. 45, pp. 18–40, 2018.

[5] M. Saifuzzaman and Z. Zheng, "Incorporating human-factors in car-following models: A review of recent developments and research needs," *Transportation Research Part C: Emerging Technologies*, vol. 48, pp. 379–403, 2014.

[6] H. Zhang, J. Peng, H. Dong, H. Tan, and F. Ding, "Hierarchical reinforcement learning based energy management strategy of plug-in hybrid electric vehicle for ecological car-following process," *Applied Energy*, vol. 333, p. 120599, 2023.

[7] J. I. Ge and G. Orosz, "Optimal control of connected vehicle systems with communication delay and driver reaction time," *IEEE Transactions on Intelligent Transportation Systems*, vol. 18, no. 8, pp. 2056–2070, 2017.

[8] S. E. Li, Q. Guo, L. Xin, B. Cheng, and K. Li, "Fuel-saving servo-loop control for an adaptive cruise control system of road vehicles with step-gear transmission," *IEEE Transactions on Vehicular Technology*, vol. 66, no. 3, pp. 2033–2043, 2017.

[9] A. Sharma, Z. Zheng, J. Kim, A. Bhaskar, and M. Mazharul Haque, "Assessing traffic disturbance, efficiency, and safety of the mixed traffic flow of connected vehicles and traditional vehicles by considering human factors," *Transportation Research Part C: Emerging Technologies*, vol. 124, p. 102934, 2021.

[10] L. Zhu, F. Tao, Z. Fu, H. Sun, B. Ji, and Q. Chen, "Multiobjective optimization of safety, comfort, fuel economy, and power sources durability for fchev in car-following scenarios," *IEEE Transactions on Transportation Electrification*, vol. 9, no. 1, pp. 1797–1808, 2023.

[11] Y. Jia, R. Jibrin, and D. Görges, "Energy-optimal adaptive cruise control for electric vehicles based on linear and nonlinear model predictive control," *IEEE Transactions on Vehicular Technology*, vol. 69, no. 12, pp. 14 173–14 187, 2020.

[12] X. Pan, B. Chen, and S. A. Evangelou, "Optimal vehicle following strategy for joint velocity and energy management control of series hybrid electric vehicles," *IFAC-PapersOnLine*, vol. 53, no. 2, pp. 14 161–14 166, 2020.

[13] B. Li, W. Zhuang, H. Zhang, H. Sun, H. Liu, J. Zhang, G. Yin, and B. Chen, "Traffic-aware ecological cruising control for connected electric vehicle," *IEEE Transactions on Transportation Electrification*, pp. 1–1, 2023.

[14] J. Peng, Y. Fan, G. Yin, and R. Jiang, "Collaborative optimization of energy management strategy and adaptive cruise control based on deep reinforcement learning," *IEEE Transactions on Transportation Electrification*, vol. 9, no. 1, pp. 34–44, 2023.

[15] J. Li, Y. Liu, Y. Zhang, Z. Lei, Z. Chen, and G. Li, "Data-driven based eco-driving control for plug-in hybrid electric vehicles," *Journal of Power Sources*, vol. 498, p. 229916, 2021.

[16] Y. Zheng, S. E. Li, J. Wang, L. Y. Wang, and K. Li, "Influence of information flow topology on closed-loop stability of vehicle platoon with rigid formation," in *17th International IEEE Conference on Intelligent Transportation Systems (ITSC)*, 2014, pp. 2094–2100.

[17] S. Zhang, Y. Luo, J. Wang, X. Wang, and K. Li, "Predictive energy management strategy for fully electric vehicles based on preceding vehicle movement," *IEEE Transactions on Intelligent Transportation Systems*, vol. 18, no. 11, pp. 3049–3060, 2017.

[18] D. Mayne, "Nonlinear model predictive control: Challenges and opportunities," in *Nonlinear Model Predictive Control*, F. Allgöwer and A. Zheng, Eds. Basel: Birkhäuser Basel, 2000, pp. 23–44.

[19] J. Hu, P. Bhowmick, F. Arvin, A. Lanzon, and B. Lennox, "Cooperative control of heterogeneous connected vehicle platoons: An adaptive leader-following approach," *IEEE Robotics and Automation Letters*, vol. 5, no. 2, pp. 977–984, 2020.

[20] R. Bravo and M. Dokainish, "Non-linear trajectory control of flexible joint manipulators," in *Current Advances in Mechanical Design and Production VII*, M. F. HASSAN and S. M. MEGAHED, Eds. Oxford: Pergamon, 2000, pp. 37–44.

[21] A. I. Rabinowitz, C. C. Ang, Y. H. Mahmoud, F. M. Araghi, R. T. Meyer, I. Kolmanovsky, Z. D. Asher, and T. H. Bradley, "Real-time implementation comparison of urban eco-driving controls," *IEEE Transactions on Control Systems Technology*, pp. 1–15, 2023.

[22] C. Pan, A. Huang, L. Chen, Y. Cai, L. Chen, J. Liang, and W. Zhou, "A review of the development trend of adaptive cruise control for ecological driving," *Proceedings of the Institution of Mechanical Engineers, Part D: Journal of Automobile Engineering*, vol. 236, no. 9, pp. 1931–1948, 2022.

[23] A. Hadjigeorgiou and S. Timotheou, "Real-time optimization of fuel-consumption and travel-time of CAVs for cooperative intersection crossing," *IEEE Transactions on Intelligent Vehicles*, vol. 8, no. 1, pp. 313–329, 2023.

[24] X. Pan, B. Chen, S. Timotheou, and S. A. Evangelou, "A convex optimal control framework for autonomous vehicle intersection crossing," *IEEE Transactions on Intelligent Transportation Systems*, vol. 24, no. 1, pp. 163–177, 2023.

[25] R. Lacombe, S. Gros, N. Murgovski, and B. Kulcsár, "Distributed eco-driving control of a platoon of electric vehicles through riccati recursion," *IEEE Transactions on Intelligent Transportation Systems*, vol. 24, no. 3, pp. 3048–3063, 2023.

[26] X. Pan, B. Chen, L. Dai, S. Timotheou, and S. A. Evangelou, "A hierarchical robust control strategy for decentralized signal-free intersection management," *IEEE Transactions on Control Systems Technology*, vol. 31, no. 5, pp. 2011–2026, 2023.

[27] F. Dong, X. Zhao, and Y.-H. Chen, "Optimal longitudinal control for vehicular platoon systems: Adaptiveness, determinacy, and fuzzy," *IEEE Transactions on Fuzzy Systems*, vol. 29, no. 4, pp. 889–903, 2021.

[28] J. Wang, X. Luo, L. Wang, Z. Zuo, and X. Guan, "Integral sliding mode control using a disturbance observer for vehicle platoons," *IEEE Transactions on Industrial Electronics*, vol. 67, no. 8, pp. 6639–6648, 2020.

[29] S. Boddupalli, A. S. Rao, and S. Ray, "Resilient cooperative adaptive cruise control for autonomous vehicles using machine learning," *IEEE Transactions on Intelligent Transportation Systems*, vol. 23, no. 9, pp. 15 655–15 672, 2022.

[30] X. Tang, J. Chen, K. Yang, M. Toyoda, T. Liu, and X. Hu, "Visual detection and deep reinforcement learning-based car following and energy management for hybrid electric vehicles," *IEEE Transactions on Transportation Electrification*, vol. 8, no. 2, pp. 2501–2515, 2022.

[31] S. Zhao and K. Zhang, "A distributionally robust stochastic optimization-based model predictive control with distributionally robust chance constraints for cooperative adaptive cruise control under uncertain traffic conditions," *Transportation Research Part B: Methodological*, vol. 138, pp. 144–178, 2020.

[32] X. Lin and D. Görges, "Robust model predictive control of linear systems with predictable disturbance with application to multiobjective adaptive cruise control," *IEEE Transactions on Control Systems Technology*, vol. 28, no. 4, pp. 1460–1475, 2020.

[33] S. Feng, Z. Song, Z. Li, Y. Zhang, and L. Li, "Robust platoon control in mixed traffic flow based on tube model predictive control," *IEEE Transactions on Intelligent Vehicles*, vol. 6, no. 4, pp. 711–722, 2021.

[34] S. Yu, X. Pan, A. Georgiou, B. Chen, I. M. Jaimoukha, and S. A. Evangelou, "Robust model predictive control framework for energy-optimal adaptive cruise control of battery electric vehicles," in *2022 European Control Conference (ECC)*. IEEE, 2022, pp. 1728–1733.

[35] S. Yu, X. Pan, A. Georgiou, B. Chen, I. M. Jaimoukha, and S. A. Evangelou, "A robust model predictive control framework for ecological adaptive cruise control strategy of electric vehicles," in *2023 IEEE International Conference on Mechtronics (ICM)*. IEEE, 2023, pp. 1–6.

[36] A. Georgiou, F. Tahir, I. M. Jaimoukha, and S. A. Evangelou, "Computationally efficient robust model predictive control for uncertain system using causal state-feedback parameterization," *IEEE Transactions on Automatic Control*, vol. 68, no. 6, pp. 3822–3829, 2023.

[37] G. Guo, Z. Zhao, and R. Zhang, "Distributed trajectory optimization and fixed-time tracking control of a group of connected vehicles," *IEEE Transactions on Vehicular Technology*, vol. 72, no. 2, pp. 1478–1487, 2023.

[38] S. Jones, N. Wikström, A. F. Parrilla, R. Patil, E. Kural, A. Massoner, and A. Grauers, "Energy-efficient cooperative adaptive cruise control strategy using V2I," in *2019 6th International Conference on Control, Decision and Information Technologies (CoDIT)*, 2019, pp. 1420–1425.

[39] L. Xu, X. Jin, Y. Wang, Y. Liu, W. Zhuang, and G. Yin, "Stochastic stable control of vehicular platoon time-delay system subject to random switching topologies and disturbances," *IEEE Transactions on Vehicular Technology*, vol. 71, no. 6, pp. 5755–5769, 2022.

[40] D. Sun, Y. Kang, and S. Yang, "A novel car following model considering average speed of preceding vehicles group," *Physica A: Statistical Mechanics and its Applications*, vol. 436, pp. 103–109, 2015.

[41] E. Hyeon, J. Han, D. Shen, D. Karbowski, N. Kim, and A. Rousseau, "Potential energy saving of V2V-connected vehicles in large-scale traffic," *IFAC-PapersOnLine*, vol. 55, no. 24, pp. 78–83, 2022, 10th IFAC Symposium on Advances in Automotive Control AAC 2022.

[42] H. He, Y. Wang, R. Han, M. Han, Y. Bai, and Q. Liu, "An improved MPC-based energy management strategy for hybrid vehicles using V2V and V2I communications," *Energy*, vol. 225, p. 120273, 2021.

[43] Y. Zhang, Y. Bai, M. Wang, and J. Hu, "Cooperative adaptive cruise control with robustness against communication delay: An approach in the space domain," *IEEE Transactions on Intelligent Transportation Systems*, vol. 22, no. 9, pp. 5496–5507, 2021.

[44] D. R. Lopes and S. A. Evangelou, "Energy savings from an eco-cooperative adaptive cruise control: a BEV platoon investigation," in *2019 18th European Control Conference (ECC)*, 2019, pp. 4160–4167.

[45] J. A. Ejsmont, G. Ronowski, B. Świeczko Żurek, and S. Sommer, "Road texture influence on tyre rolling resistance," *Road Materials and Pavement Design*, vol. 18, no. 1, pp. 181–198, 2017.
[46] B. Chen, S. A. Evangelou, and R. Lot, "Series hybrid electric vehicle simultaneous energy management and driving speed optimization," *IEEE/ASME Transactions on Mechatronics*, vol. 24, no. 6, pp. 2756–2767, 2019.
[47] T. Markel, A. Brooker, T. Hendricks, V. Johnson, K. Kelly, B. Kramer, M. O'Keefe, S. Sprik, and K. Wipke, "ADVISOR: a systems analysis tool for advanced vehicle modeling," *Journal of Power Sources*, vol. 110, no. 2, pp. 255–266, 2002.
[48] J. L. Jerez, E. C. Kerrigan, and G. A. Constantinides, "A sparse and condensed QP formulation for predictive control of LTI systems," *Automatica*, vol. 48, no. 5, pp. 999–1002, 2012.
[49] D. Mayne, J. Rawlings, C. Rao, and P. Scokaert, "Constrained model predictive control: Stability and optimality," *Automatica*, vol. 36, no. 6, pp. 789–814, 2000.
[50] F. Tahir and I. M. Jaimoukha, "Causal state-feedback parameterizations in robust model predictive control," *Automatica*, vol. 49, no. 9, pp. 2675–2682, 2013.
[51] J. Löfberg, "Yalmip : a toolbox for modeling and optimization in matlab," in *2004 IEEE International Conference on Robotics and Automation (IEEE Cat. No.04CH37508)*, 2004, pp. 284–289.
[52] MOSEK ApS, *MOSEK Optimization Toolbox for MATLAB 10.0.43*, 2023. [Online]. Available: https://docs.mosek.com/10.0/toolbox/index.html
[53] J. Guo, H. He, and C. Sun, "Arima-based road gradient and vehicle velocity prediction for hybrid electric vehicle energy management," *IEEE Transactions on Vehicular Technology*, vol. 68, no. 6, pp. 5309–5320, 2019.
[54] K. N. de Winkel, T. Irmak, R. Happee, and B. Shyrokau, "Standards for passenger comfort in automated vehicles: Acceleration and jerk," *Applied Ergonomics*, vol. 106, p. 103881, 2023.

Sheng Yu (Student Member, IEEE) received the M.Eng. degree in electrical and electronic engineering from the Department of Electrical and Electronic Engineering, Imperial College London, London, U.K., in 2021, where he is currently pursuing the Ph.D. degree. His research focuses on the optimisation of autonomous driving for electric vehicles, robust model predictive control, and game-theoretical control.

Xiao Pan received the B.Sc. degree in automation from the Xu Teli School, Beijing Institute of Technology, Beijing, China, in 2017, and the M.Sc. degree in control system (Hons.) and Ph.D. degree in electrical and electronic engineering research from the Department of Electrical and Electronic Engineering, Imperial College London, London, U.K., in 2018 and 2023, respectively. His research interests include modelling, control, and optimisation theory on automated and electric vehicles.

Anastasis Georgiou (Member, IEEE) received the B.Sc. degree in Electrical and Computer Engineering from the University of Cyprus, Cyprus, in 2015. He joined Imperial College London in 2016 and he completed his M.Sc. and Ph.D. degrees in Control Systems from the Department of Electrical and Electronic Engineering in 2017 and 2022, respectively. From 2022 to 2023, he was a Postdoctoral Research Associate within the Department of Mechanical Engineering at the University of Minnesota-Twin Cities. Currently, he is a Senior Controls Engineer with Nikola Motor Company, USA. His research interests include dynamic system modelling, robust control and estimation design and its applications to robotics and automotive industry.

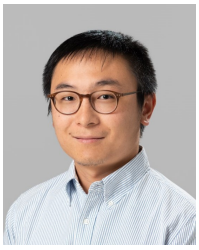

Boli Chen (Member, IEEE) received the B. Eng. in Electrical and Electronic Engineering in 2010 from Northumbria University, UK. In 2011 and 2015, he respectively received the MSc and the Ph.D. in Control Systems from Imperial College London, UK. Currently, he is a Lecturer in the Department of Electronic and Electrical Engineering, University College London, U.K. He is also an associate editor of the European Journal of Control and an associate editor of the EUCA Conference Editorial Board. He has research interests in control, optimisation and estimation of complex dynamical systems, with applications focusing on the automotive, transportation and electric energy systems.

Imad M. Jaimoukha received the B.Sc. degree in electrical engineering from the University of Southampton, Southampton, U.K., in 1983, and the M.Sc. and Ph.D. degrees in control systems from the Imperial College London (ICL), London, U.K., in 1986 and 1990, respectively. He was a Research Fellow with the Centre for Process Systems Engineering, ICL, from 1990 to 1994, where he has been with the Department of Electrical and Electronic Engineering since 1994. His research interests include robust and fault-tolerant control, system approximation, and global optimisation.

Simos A. Evangelou (Senior Member, IEEE) received the B.A. and M.Eng. degrees in electrical and information sciences from the University of Cambridge, Cambridge, U.K., in 1999, and the Ph.D. degree in control engineering from Imperial College London, London, U.K., in 2004. He is currently a Reader with the Department of Electrical and Electronic Engineering, Imperial College London. He serves on the Editorial Board of international journals and conferences, including the IEEE Transactions on Control Systems Technology and the IEEE Control Systems Society Conference Editorial Board.